

<https://doi.org/10.1038/s41529-025-00603-9>

A generative diffusion-based AI-model to scrutinise the microstructural degradation of isothermally aged Cu-SAC305 interfaces



Charlotte Cui¹, Fereshteh Falah Chamasemani¹, Michael Reisinger², Peter Imrich², Walter Hartner³, Werner Robl³ & Roland Brunner¹ ✉

Generative artificial intelligence (genAI) has disrupted multiple disciplines, as it has the potential to drastically change the way content is created. In this study, microstructural grey-value images of thermally aged interfacial Cu–SAC305 microstructures are virtually generated for seen, unseen and even unknown sample conditions utilising a denoised diffusion probabilistic model (DDPM). The DDPM is conditioned based on the different ageing time and impurity levels. The multi-scale structural similarity index is calculated to assess the quality of generated images. Kirkendall pore areas and IMC-thicknesses are extracted from labelled real and generated images as physical descriptors, to quantitatively characterise the microstructure. Both follow the expected physical trends of parabolic growth, confirming the underlying diffusion process and validating the pertinency of the model. Hence, this study demonstrates the feasibility of genAI to significantly enhance systematic imaging investigations of microstructural degradation with concurrently reducing experimental effort.

Generative artificial intelligence (genAI) has disrupted multiple disciplines, from daily life to education^{1–3}, medicine^{4–6}, scientific research⁷ and even art^{8,9}, as it has the potential to drastically change the way we approach content creation. In contrast to predictive algorithms, generative ones are able to create data, e.g. human-sounding text¹⁰ and photo-realistic images¹¹. GenAI describes algorithms such as large language models^{12–17}, generative adversarial networks (GANs)^{18–20} or denoised diffusion probabilistic models (DDPMs)^{20,24}, which have emerged as revolutionary approaches allowing the generation of realistic and diverse data, including text, audio, code, images, simulations and videos. In this context, GANs and DDPMs have shown high potential for AI-based image generation^{19,20,23}. However, GAN-based models exhibit challenges related to training complexity, mode collapse, application domain limitation and restrictions in image generation diversity. Moreover, GANs demand rather large datasets for their training^{18,20,23,24}. More recently developed DDPMs are able to surpass GANs in image synthesis. DDPMs have shown their potential in various domains, including natural language processing, computer vision, robust machine learning, interdisciplinary applications in medical image reconstruction and computational chemistry^{24–29}. Moreover, DDPMs are altering the approach for visualisation and analysis of microstructures of materials, generating

high-quality, diverse images that have the potential to enhance our understanding of material properties and behaviours, leading to advancements in material design and application^{20,23,28}. Conditional DDPMs (C-DDPMs) extend the architecture of standard DDPMs by incorporating additional conditioning information, such as class labels, text descriptions or other modalities, which enables more controlled and relevant image generation^{20,23,30}. Yet, as true for all generative models, validation of the virtually generated image data is indispensable. AI hallucination needs to be identified and eliminated^{31–33}. In materials science, physical descriptors like microstructural features can be used for the validation of generative models^{20,34}. Therefore, a comparison of such features in real and generated images in the context of the underlying physical trends is suitable to assess genAI outputs²⁰.

The ever-growing need for the integration of more components on a single chip and improved functionality, while reducing overall device size in microelectronic packaging, strongly impacts interconnects in the context of structural integrity and their electrical and thermal conductivity^{35,36}. Recently, machine learning in combination with sophisticated imaging methods has showcased possibilities for the statistical evaluation of defects in modern interconnect technologies^{37–41}. The electric interconnection of

¹Materials Center Leoben Forschung GmbH, Leoben, Austria. ²Kompetenzzentrum für Automobil- und Industrielektronik GmbH, Villach, Austria. ³Infineon Technologies AG, Regensburg, Germany. ✉e-mail: roland.brunner@mcl.at

individual electronic building blocks is achieved via metallisations. Copper (Cu) is commonly utilised for the metallisation in microelectronic devices due to its high thermal and electrical conductivity^{42–47}. There are various ways to fabricate the Cu metallisation on the backside of a chip. One way is to grow the metallisation via physical vapour deposition (PVD), which yields a metallisation with high-purity⁴⁸. Another established fabrication route is growing electro-chemically deposited (ECD-) Cu on a PVD-Cu seed-layer⁴⁸. The ECD route involves the deposition of Cu in a liquid electrolyte from an organic complex onto the cathode, i.e. the chip, by applying voltage to the electrodes^{35,44}. Therein, the growth rate of the metallisation is largely dependent on the current density during deposition^{35,49}. In addition to the Cu-complexes, the electrolyte contains a variety of additives to control the growth of the metallisation³⁵. These electrolyte additives may be incorporated into the metallisation as impurities and ultimately affect the functionality of the device. The extent to which that occurs is dependent, among other things, on the current density during deposition, i.e. the speed of ECD-Cu metallisation growth^{35,49}. One space-saving type of interconnect is a ball grid array, wherein solder balls³⁷ ensure both electrical and thermal connection between the chip and printed circuit board (PCB). The interconnect is usually composed of a low-melting metal alloy, since the joining of the microelectronic building blocks should be thermally as non-invasive as possible^{42,50,51}. Some of the most popular solder alloys to replace Lead-based solders in microelectronics are from the family of Tin- (Sn-) based ternary eutectics with Silver (Ag) and Cu^{42,52–55}. Within this family of alloys, the Sn–3.0 wt.% Ag–0.5 wt.% Cu (SAC305) alloy has proven to be one viable choice in terms of its processability^{56–59} and mechanical integrity^{42,59–61}. The microstructure of such a SAC305 solder alloy consists of the intermetallic compounds (IMCs) Cu_6Sn_5 and Ag_3Sn , which are embedded in a β -Sn matrix^{42,52–55}. During reflow, layers of IMCs form between the Cu metallisation and the SAC305 solder ball due to liquid–solid interdiffusion, namely Cu_3Sn on the Cu-rich side and Cu_6Sn_5 on the Sn-rich side^{35,44,45,62–64}. These IMC-layers continue to grow due to solid-state Cu–Sn interdiffusion when the device is thermally aged^{144–46,62,65}. During ageing, impurities that are potentially incorporated into the ECD-Cu metallisation also take part in the interdiffusion. These impurities throw the Cu–Sn interdiffusion out of balance, and lead to the formation of Kirkendall pores within the Cu_3Sn -layer^{35,44,49,66}. Studies about the influence of Cu-impurities on the Kirkendall pore formation have been performed to some extent previously^{35,45,49,66–69}. However, systematic and comprehensive imaging of the effects of various impurity contents on the interfacial Cu–SAC305 microstructure over multiple ageing timesteps demands substantial experimental effort. Because experimental microstructural imaging of such complex sample datasets is time-consuming and labour-intensive, incomplete or incomparable datasets may result. With the advancement of genAI algorithms in recent years^{30,70,71}, and their ability to generate image data, unlike non-generative algorithms, e.g. ML-based image classification algorithms^{37,38,72–74}, opportunities to fill the data gap are opening up.

Therefore, our study intends to highlight the implementation of genAI to facilitate efficient and systematic in-depth investigations of isothermally aged interfacial Cu–SAC305 microstructures. The genAI algorithm is based on a conditional- (C-) DDPM, which is conditioned by the ageing time and ECD-Cu metallisation growth rates, which correlate with the Cu-impurity contents. As a high-purity reference, a PVD-Cu metallisation is also studied. Moreover, the diffusion parameters of the C-DDPM are tuned to generate high-quality microstructural images of Cu–SAC305 interfaces for seen, unseen, as well as unknown conditions. The developed C-DDPM is able to generate microstructural images that are qualitatively indistinguishable from real field emission scanning electron microscopy backscatter electron (FESEM-BSE) micrographs, although trained on relatively few training data. The image quality of generated images for seen and unseen conditions is assessed by calculating the multi-scale structural similarity index (MS-SSIM). The MS-SSIM yields 0.79, indicating high similarity to real FESEM-BSE micrographs in terms of brightness, contrast, as well as texture⁷⁵. The C-DDPM's ability to generate physically accurate microstructural images for given sample conditions is assessed by the evaluation of physical descriptors,

i.e. microstructural features like IMC-layer thicknesses and Kirkendall pore areas. These microstructural features are extracted from labelled FESEM-BSE micrographs as well as from labelled generated image data and subsequently compared. A quantitative comparison of the evaluated microstructural features reveals that the virtually generated data generally lies within the standard deviations of the real data. Furthermore, we show that the evaluated physical quantities, such as the parabolic growth rates of the IMC layers and Kirkendall pore areas, are dependent on the Cu-impurity content. The reduction of Kirkendall pore formation enthalpy with increasing impurity content is estimated from both real and generated image data. We confirm that, based on the evaluated physical descriptors, the C-DDPM is also able to generate microstructural images for given unknown sample conditions, i.e. conditions where no experimental data is available. The depicted features follow the expected trends from the underlying physical interdiffusion mechanisms. Hence, this study demonstrates the potential of a C-DDPM to significantly reduce experimental efforts for microstructural visualisations and studies of degradation mechanisms by implementing genAI.

Results

Impact of balanced and imbalanced Cu–Sn interdiffusion on the interfacial IMC microstructure during isothermal ageing

Electronic devices may be exposed to elevated temperatures during their service. The microstructural changes in Sn-based solder ball interconnects due to these elevated temperatures may have adverse effects on the performance and functionality of the device. A 3D X-ray tomography reconstruction of such an electronic device is shown in Fig. 1a, wherein a 3×3 solder ball grid array is visible, as well as the Cu metallisation of the chip on top and of the PCB beneath. A FESEM-BSE cross-sectional overview of an exemplary solder ball is depicted in Fig. 1b. Since the growth of the interfacial IMC-layers is caused by the interdiffusion of Sn and Cu, their evolution is largely dependent on the ageing time and temperature^{69,76,77}. The growth of interfacial IMCs during isothermal ageing, schematically shown in Fig. 1c, may also impact mechanical and electrical properties of the interface. The schematic depicts the evolution of the interface assuming balanced Cu and Sn interdiffusion. If the Cu–Sn interdiffusion is imbalanced, as is the case when impurities are incorporated in the Cu metallisation, Kirkendall pore formation is expected. This case is schematically shown in Fig. 1d. In general, pore formation is associated to an increase in both the electrical as well as the thermal resistance^{20,78}. This relationship may also be applicable for the observed nano-scale Kirkendall pores.

Real micrographs of the conditions in Fig. 1c, d, namely FESEM energy dispersive X-ray spectroscopy (EDX) mappings of Cu, Sn and Ag, are shown in Fig. 1e and f. The respective exemplary EDX-mappings of the PVD-Cu metallisation, i.e. without impurities over isothermal ageing as sketched in Fig. 1c, are shown in Fig. 1e. Figure 1f shows an EDX-mapping of an ECD-Cu metallisation, i.e. with impurities, corresponding to the schematic depicted in Fig. 1d. The illustrated PVD-Cu samples with no impurities are aged at 150 °C for 0, 100 and 1000 h, respectively. The sample with impure ECD-Cu is aged for 1000 h at 150 °C. Further details about the sample fabrication and ageing, as well as X-ray tomography imaging, FESEM imaging and EDX mapping are given in 'Methods'. The various phases of interest at the interface, i.e. Cu, Cu_3Sn , Cu_6Sn_5 and the bulk of the SAC305 solder ball, can be distinguished by their contrasts in the EDX-mappings due to their decreasing Cu-contents and increasing Sn-contents, respectively. It is also shown that Ag_3Sn precipitates are embedded in the Sn matrix and that some larger ones are situated at the Cu_6Sn_5 –SAC305 interfaces.

Impact of impurity content on the interfacial microstructure during isothermal ageing

Figure 2 illustrates the experimentally evaluated sample conditions in the ageing time / Cu-impurity matrix. It shows representative snippets from cross-sectional FESEM-micrographs utilising a BSE detector, aged from 0 h up to 3000 h at 150 °C for PVD- and ECD-Cu, respectively. For the latter, various impurity incorporation into the ECD-Cu metallisation is achieved

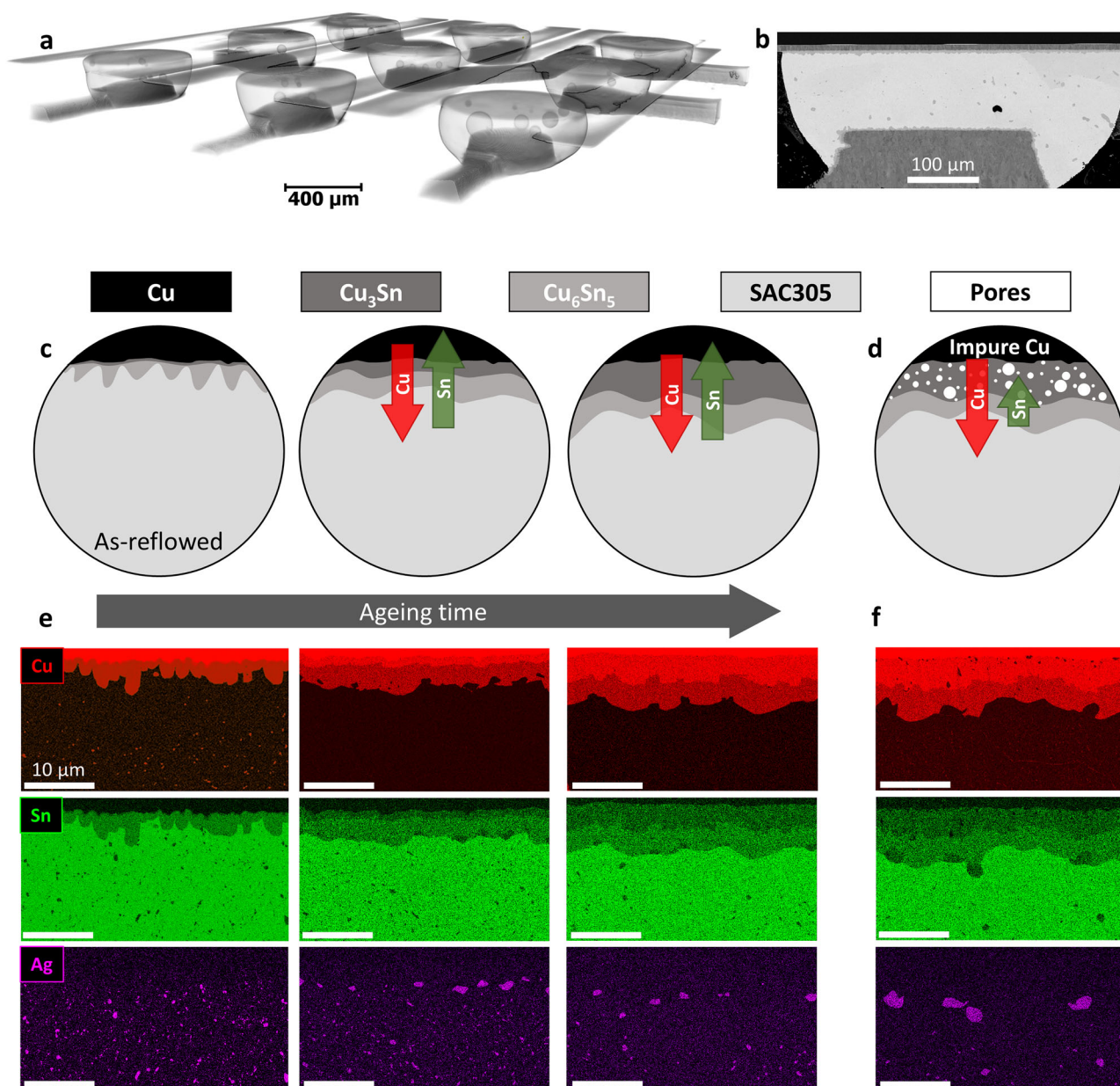


Fig. 1 | Sample overview, schematic IMC-layer growth and Kirkendall pore formation during ageing, as well as exemplary EDX mappings. Investigated sample geometry and microstructural evolution of the Cu–SAC305 interface during isothermal ageing. **a** 3D X-ray tomography scan of an exemplary investigated sample. The visualisation shows the solder balls and the Cu metallisations. **b** Exemplary FESEM-BSE overview cross-section of a solder ball. **c** Schematic IMC-layer growth with balanced interdiffusion of Cu and Sn. **d** Schematic pore formation caused by imbalanced Cu–Sn interdiffusion due to impurities in the Cu metallisation. The arrows in (**c**, **d**) schematically sketch the diffusion rates of Cu (red) and Sn (green). Cu, Cu₃Sn, Cu₆Sn₅, SAC305 and pores are depicted in exceedingly brighter

shades of grey. **e** EDX-mappings of PVD–Cu–SAC305 interfaces for Cu, Sn and Ag at exemplary ageing times of 0, 100 and 1000 h at 150 °C, corresponding to the schematic conditions in **c** with balanced Cu–Sn interdiffusion. **f** EDX-mappings of an aged ECD–Cu–SAC305 interface after 1000 h at 150 °C for Cu, Sn and Ag, corresponding to the schematic in **d** with imbalanced Cu–Sn interdiffusion. The Cu signal is shown in red, Sn in green and Ag in purple. Cu, Cu₃Sn, Cu₆Sn₅ and the SAC305 bulk can be distinguished due to their decreasing Cu-content and their increasing Sn-content, respectively. Kirkendall pores appear black in the Cu₃Sn-layer. Ag₃Sn-precipitates are embedded into the Sn-matrix and at the Cu₆Sn₅–SAC305 interface. Scalebar of 10 µm is valid for all images.

by applying three different current densities, resulting in different growth rates. Three current densities are studied, which are listed in Supplementary Table 1. The FESEM-BSE-micrographs allow the distinction of the occurring phases like Cu, Cu₃Sn, Cu₆Sn₅ and the SAC305 bulk due to mass-contrast. Cu is shown to be the darkest phase, followed by Cu₃Sn and Cu₆Sn₅. The SAC305 bulk exhibits the brightest grey value, whereas Kirkendall pores appear black. Each column in Fig. 2 represents one isothermal ageing timestep at 150 °C and each row corresponds to one Cu metallisation impurity content. PVD-Cu is assumed to contain the least amount of impurities and is therefore considered as reference. The impurity contents of

the ECD-Cu metallisations are defined via their deposition parameters, specifically, by the applied current densities during deposition. The metallisations of the samples ECD1, ECD2 and ECD3 are deposited with increasing current densities, see Supplementary Table 1. Increasing current densities correlate with increasing incorporation of impurities into the Cu metallisations^{35,49}. The PVD- and ECD2-samples are aged for 0 (as-reflowed), 50, 100, 300, 1000 and 3000 h at 150 °C, whereas the ECD1- and ECD3-samples are aged for 0, 750 and 3000 h at 150 °C. The dataset in Fig. 2 indicates the growth of the interfacial IMC layers with increasing ageing time at 150 °C. Moreover, the increase of Kirkendall pores in the Cu₃Sn-

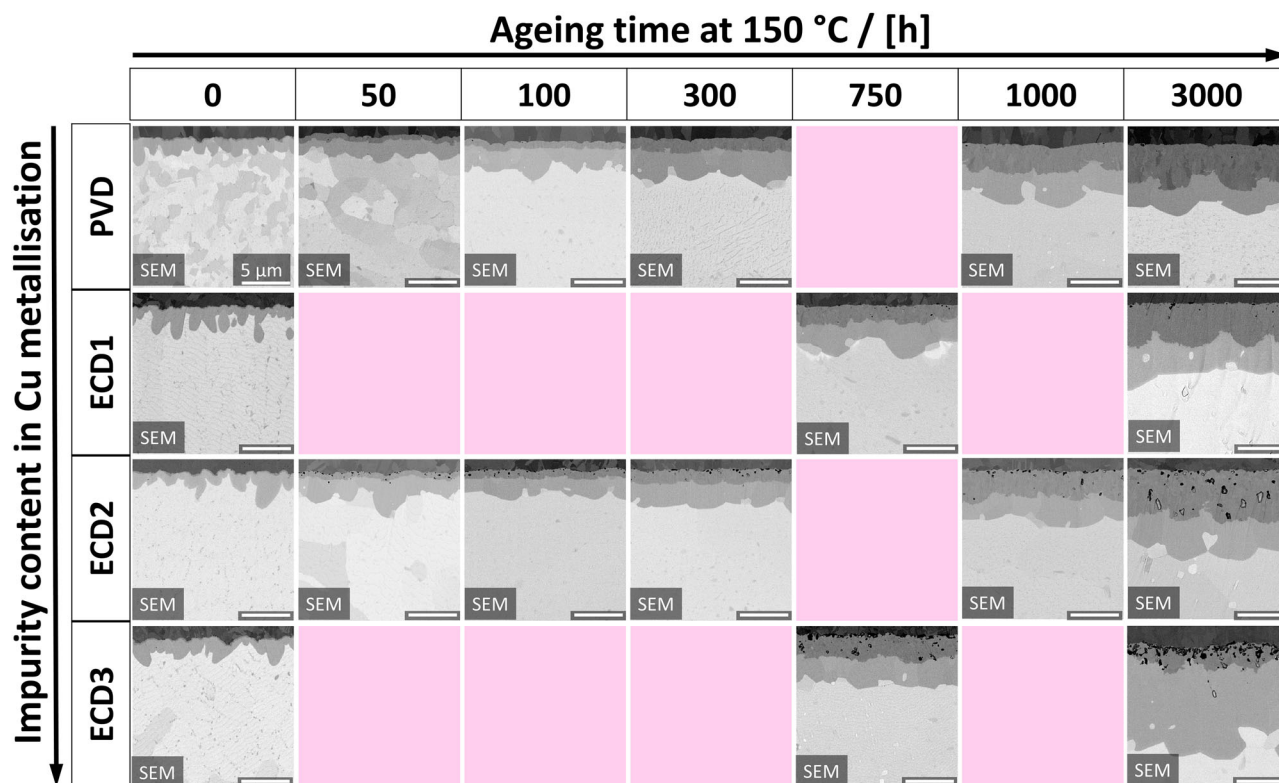


Fig. 2 | Interfacial Cu–SAC305 microstructure dependent on ageing time at 150 °C and impurity content in the Cu metallisations. Sample matrix for the Cu–SAC305 interfaces with PVD- and ECD-Cu, over isothermal ageing time at 150 °C. The ECD-Cu metallisations are grown with three different rates. For each investigated impurity content and ageing timestep, one exemplary raw FESEM-BSE micrograph is shown. Scalebar of 5 µm is valid for all images. Pink panels represent

unknown conditions. From top to bottom: increasing impurity content in the Cu metallisation. PVD-Cu corresponds to a reference with a minimal amount of impurities. ECD1, ECD2 and ECD3 correspond to electroplated Cu metallisations, deposited with increasing current densities. From left to right: increasing isothermal ageing time at 150 °C. The PVD- and ECD2-samples are aged for 0, 50, 100, 300, 1000 and 3000 h. The ECD1- and ECD3-samples are aged for 0, 750 and 3000 h.

layer with increasing deposition current densities of the Cu metallisation is apparent. Thus, the Cu–SAC305 interfacial microstructure changes significantly with increasing Cu-impurity content and ageing time, as qualitatively illustrated in the sample matrix in Fig. 2. Nevertheless, a complete understanding of the underlying degradation cannot be directly retrieved, since the matrix is incomplete. Specifically, for the PVD- and ECD2-Cu metallisation, 14% of the ageing conditions are unknown. For the ECD1- and ECD3-Cu metallisation, 57% of the ageing conditions are unknown. Note, that the experimental fabrication of a full systematic sample set as well as the subsequent FESEM imaging is highly labour-intensive and time-consuming, as sketched in Supplementary Fig. 1a. Further, it should be noted that the most time-consuming step is the ageing process, which takes up to 3000 h in this study, an equivalent of 125 days. Accelerated ageing at higher temperatures may not be feasible due to the low eutectic temperature of SAC305, see also ‘Methods’. Moreover, although FESEM-BSE imaging is less time-consuming than EDX mapping, the careful sample preparation that is crucial to gain deformation- and artefact-free cross-sections still takes a substantial amount of time. Details about the sample preparation and FESEM-BSE imaging are given in ‘Methods’.

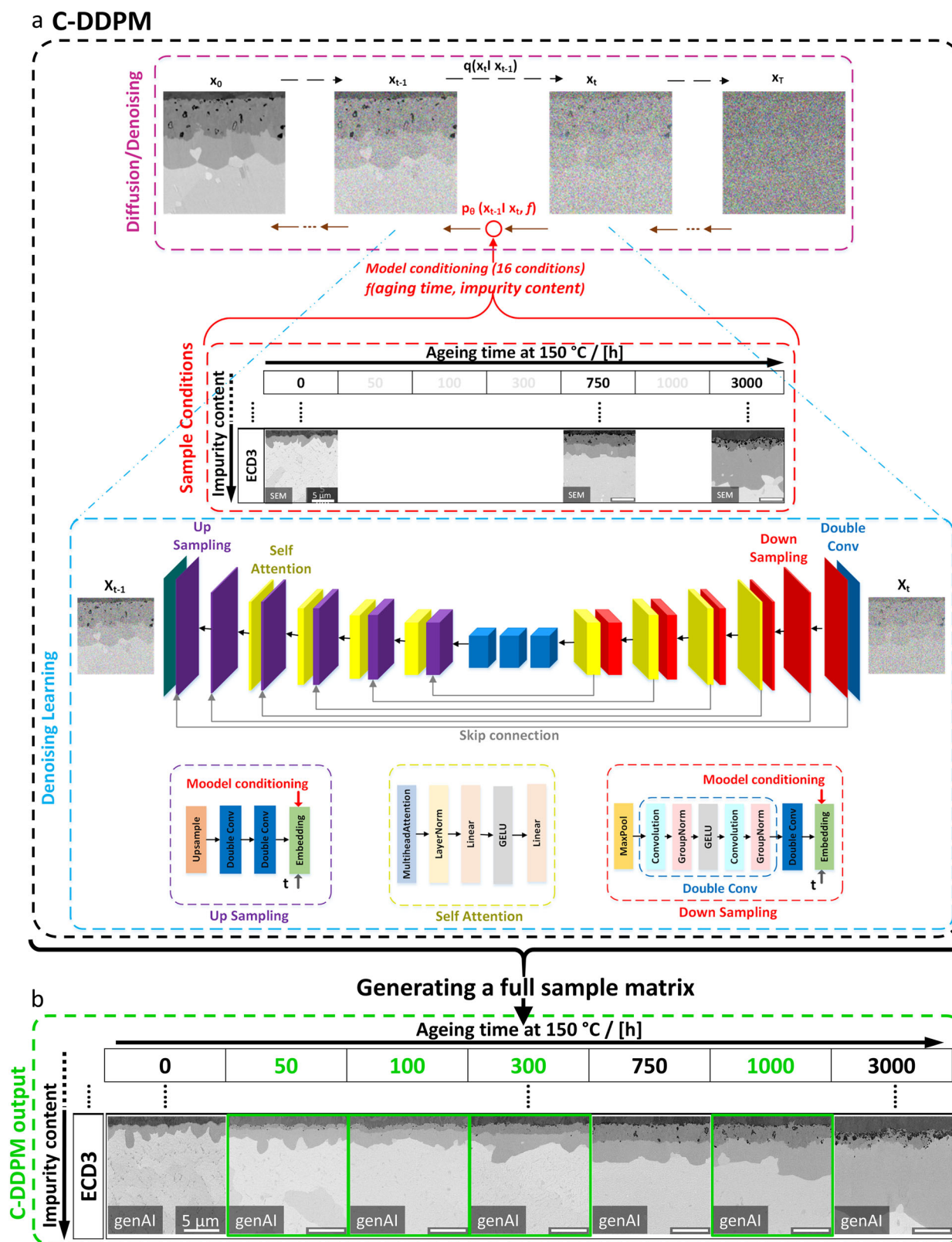
C-DDPM implementation, training and conditioning of the genAI

Figure 3 illustrates the C-DDPM, which is developed and trained to reduce experimental effort and time in terms of tedious sample production, sample preparation and FESEM imaging. During the generation of images, conditioning information is incorporated, so that the C-DDPM generates microstructural images for specific sample conditions. Sample conditions, which are included in the training data of the C-DDPM are hereafter referred to as ‘seen conditions’, see ‘Methods’. Hence, for seen conditions, the C-DDPM generates microstructural images by imitating the training data, in the ageing time/impurity matrix. The next objective is to virtually

generate microstructural images for ‘unseen conditions’, i.e. sample conditions which are experimentally available but deliberately excluded from the training data. Two specific conditions from Fig. 2, namely PVD-300 h and ECD1-750 h, are selected as unseen conditions. This approach allows the validation of the model accuracy for sample conditions that the model was not trained on.

Once the model is validated with respect to the generation of seen and unseen conditions, the ultimate goal is to virtually generate microstructural images for ‘unknown conditions’, for which experimental image data is not available, i.e. the pink panels in the sample matrix in Fig. 2. A schematic illustrating the flowchart comprising the experimental process and the approach implementing genAI is illustrated in Supplementary Fig. 1a, b. The schematic illustrates that by employing genAI, experimental fabrication and imaging efforts can be significantly reduced.

Figure 3a indicates the schematic of the C-DDPM, which consists of two Markov chains initiating stochastic processes in two directions, a forward and a reverse process. The forward chain destructs the FESEM image by progressively adding noise to the input. The reverse chain performs the denoising process, starting with pure random noise. Progressively, noise is removed to generate new image data that resembles the original image, considering specific conditioning information. Hence, the diffusion–denoising approach aims to learn the underlying data distribution, allowing the C-DDPM to denoise images from pure random noise and thereby generating new FESEM-BSE-style images which consider the given sample conditions. Exemplary images from diffusion ($q(x_t|x_{t-1})$) and denoising ($p_\theta(x_{t-1}|x_t, f)$) are illustrated in Fig. 3a. The black arrows in Fig. 3a show how the diffusion process begins with a real FESEM-BSE data, x_0 , and gradually introduces Gaussian noise across a time series x_1, x_2, \dots, x_T , wherein each step depends only on the preceding one. The denoising process is



represented by brown arrows in Fig. 3a. In order to denoise image data, the C-DDPM learns transition kernels, parameterised by the convolutional neural network U-Net architecture, and returns the noisy image samples to the data distribution.

Moreover, the model conditioning, indicated in red and exemplarily shown in Fig. 3a, is incorporated in the denoising procedure. The C-DDPM

is conditioned based on Cu-impurity contents and isothermal ageing times, which is exemplarily indicated in Fig. 3a by the red circle. Further details are provided in 'Methods'. Finally, after training and conditioning, the C-DDPM will be able to generate microstructural images of unknown sample conditions, as exemplarily shown in Fig. 3b for ECD3. Here, the generated images of unknown conditions are highlighted in green. For each

Fig. 3 | Schematic structure, model conditioning and exemplary images from the noising/denoising sequence of the developed C-DDPM. **a** Exemplary 512×512 pixels² images from diffusion and denoising, wherein x_0 represents the raw FESEM-BSE micrograph. Model conditioning is performed utilising 16 sample conditions from Fig. 2, partially shown for the experimentally available ageing timesteps of ECD3, i.e. 0, 750 and 3000 h. The schematic structure of the denoising learning U-Net is shown. The C-DDPM possesses a modified self-attention U-Net structure with seven layers for denoising learning. The self-attention blocks are shown in yellow, the down-sampling blocks of the encoder in red, the up-sampling blocks of the decoder in purple and convolutional layers in blue. The detailed structures of the

up-sampling, self-attention and down-sampling blocks are illustrated in the purple, yellow and red dashed boxes, respectively. Skip connections between encoder and decoder are shown as grey arrows. Between each denoising sequence, this model is applied to the image. In the self-attention and down-sampling blocks, GELU describes Gaussian error linear unit activation functions. **b** Exemplary outputs from the C-DDPM for ECD3. Microstructural images of known conditions from (a) are generated, as well as missing sample conditions are generated for 50, 100, 300 and 1000 h, marked in green. The full ageing time/Cu-impurity matrix of generated microstructural images is shown in Supplementary Fig. 2.

sample condition, regardless of seen, unseen or unknown, three images are generated utilising the C-DDPM. The full ageing time/Cu-impurity matrix of exemplary generated microstructural images is shown in Supplementary Fig. 2. Hence, after training and conditioning, the C-DDPM ultimately generates microstructural images for unknown sample conditions to fill up the sample matrix from Fig. 2.

Testing and validating the C-DDPM for experimentally available seen and unseen conditions

The trained C-DDPM from Fig. 3 is utilised to generate microstructural images of Cu-SAC305 interfaces for each experimentally available seen and unseen condition. Three images are generated for each condition in order to gain more statistical insight into the image generation by the C-DDPM from random noise. Subsequently, the model is validated based on how well the generated microstructural features quantitatively obey the underlying physical mechanisms, which are expressed in the real FESEM-BSE micrographs. From these generated images, microstructural features are extracted for the physics-based model validation. The corresponding workflow is sketched in Fig. 4a. The first and second rows in Fig. 4b, c show the real FESEM-BSE micrographs and generated images for a selection of seen conditions and the two unseen conditions, respectively. Qualitatively, the generated images imitate the real FESEM-BSE micrographs well in terms of resolution, contrast and realism of microstructural features. This is true for seen, as well as unseen, conditions. The MS-SSIM is calculated for a quantitative determination, whether the generated images look like real FESEM-BSE micrographs, in terms of brightness, contrast and texture, see 'Methods'. The calculated MS-SSIM yields 0.79, indicating high resemblance to the real FESEM-BSE micrographs⁷⁵.

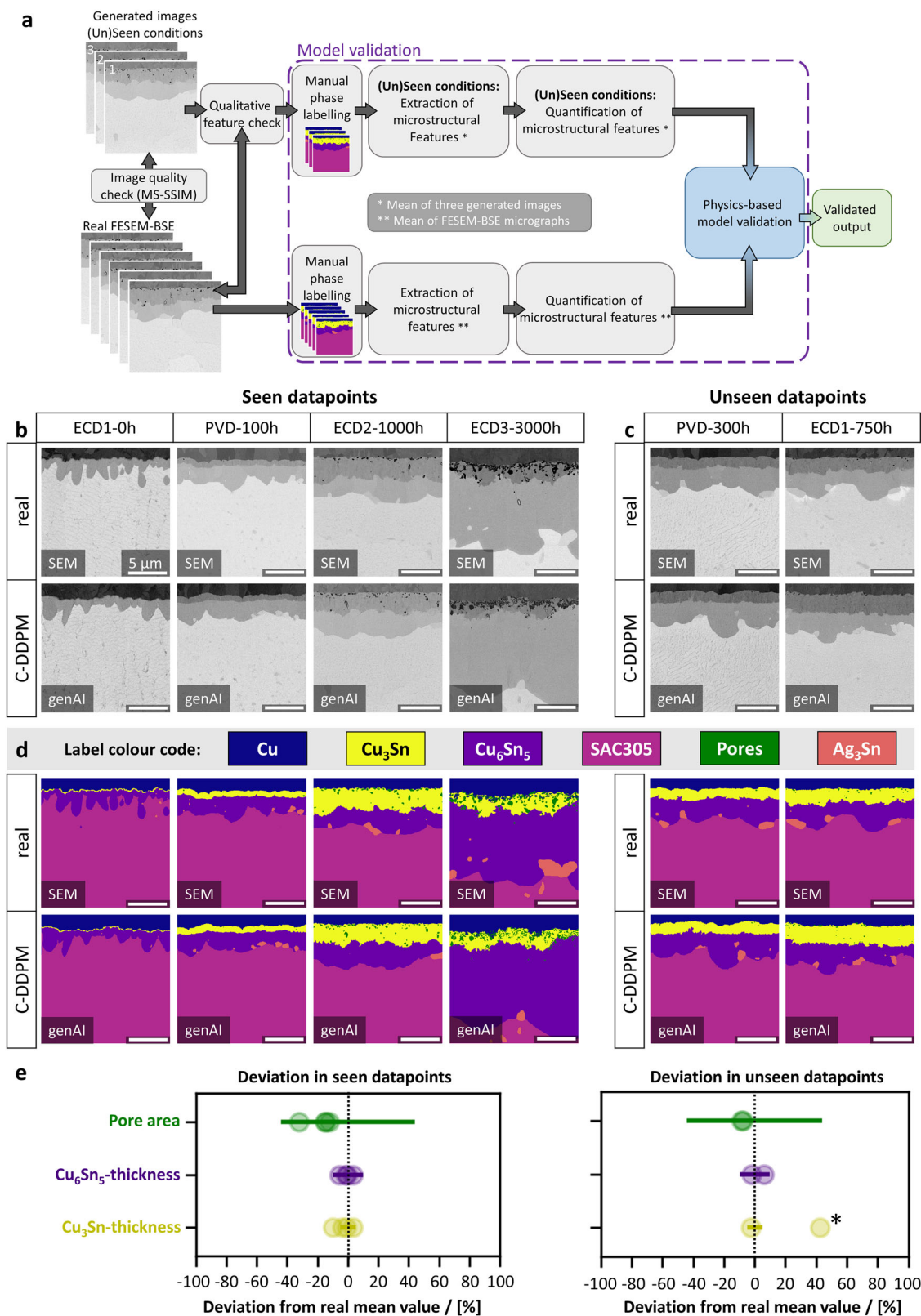
Further, quantitative analysis of the deviation between the generated and real microstructure is essential for an objective validation^{20,34}. Hence, the model is validated utilising a physics-based approach incorporating physical descriptors, in order to ensure that the microstructural features depicted in the generated images comply with the underlying physical mechanisms²⁰. Specifically, IMC-layer growths and Kirkendall pore area increase are quantified for generated images and compared to those of real FESEM-BSE micrographs for each sample condition, as sketched in Fig. 4a. For the quantification, the features of interest are labelled in both real FESEM-BSE micrographs and C-DDPM images after their generation utilising ilastik⁷⁹, as described in 'Methods'. Exemplary labelled image data is shown in Fig. 4d for the corresponding microstructural images in Fig. 4b, c. In the labelled images, the phases of interest are segmented, i.e. Cu, Cu₃Sn, Cu₆Sn₅, SAC305 bulk, Kirkendall pores and Ag₃Sn-precipitates adjacent to the IMC-layers. From these phase labels, quantitative microstructural information can be extracted. In particular, the mean Cu₃Sn- and Cu₆Sn₅-thicknesses are calculated for each image, as well as the Kirkendall pore areas. Details about IMC-thickness and pore area calculations are given in 'Methods'. A complete dataset matrix for all experimentally available conditions, seen and unseen, of real and generated images is shown in Supplementary Fig. 3, and a complete matrix of the corresponding labels is provided in Supplementary Fig. 4. The degrees which these microstructural features obey the underlying physical mechanisms are utilised as accuracy metrics. Thus, it is determined how well the C-DDPM is able to learn the underlying physical mechanisms which drive these microstructural changes. In Fig. 4e, the deviations between microstructural features depicted in generated images and their real

mean values of the FESEM-BSE micrographs are calculated for each Cu-impurity content and compared to the standard deviations in the real micrographs. In particular, the analysis is done for the Kirkendall pore area and the Cu₆Sn₅- and the Cu₃Sn-thickness. The data is plotted separately for seen and unseen conditions. The corresponding numerical values for the deviations are given in Supplementary Table 2. Details about the analysis are given in 'Methods'. Moreover, real mean values and standard deviations, as well as mean values of generated images for Kirkendall pore areas, Cu₆Sn₅-thicknesses and Cu₃Sn-thicknesses are given in Supplementary Tables 3–5, respectively. The analysis shows that the pore areas, Cu₃Sn- and Cu₆Sn₅-thicknesses in the generated images lie well within the standard deviations of the respective real micrographs for seen conditions. For unseen datapoints, the pore areas and Cu₆Sn₅-thicknesses in generated images lie within the standard deviations of the respective real conditions. While the Cu₃Sn-thickness is correctly generated for the unseen condition PVD-300 h, it is slightly over-estimated for the unseen condition ECD1-750 h, which is shown in Supplementary Table 5 and marked with an asterisk in Fig. 4e. It should be noted that there is very little experimental data available for the ECD1-Cu metallisation, and also for the ageing timestep at 750 h. In fact, there are only two other ageing timesteps for the ECD1 sample and only one other sample, ECD3, aged for 750 h. Still, although the developed C-DDPM produces slight misestimates the quantitative magnitudes of individual features, as shown in Fig. 4e and Supplementary Tables 2–5, the overall trends for IMC-layer growth and Kirkendall pore formation follow the expected underlying physical mechanisms. This can be qualitatively seen in Fig. 4b–d, Supplementary Fig. 3 and Supplementary Fig. 4, as the IMC-layer thicknesses increase with increasing ageing time and the Kirkendall pore areas increase with increasing Cu-impurity content. In order to determine potential differences in the smoothness of the Cu₆Sn₅ – SAC305 interfaces, we calculate the line length from the labelled real and virtually generated images for different conditions. The comparison demonstrates that the line length deviates by only a maximum of 8%, indicating high similarity between both. See also Supplementary Fig. 5 for further information.

Note that we also compared the performance of C-DDPM to a C-GAN model. Contrary to the training of the C-DDPM, no sample conditions are excluded from the training of the C-GAN, since the applied C-GAN can only generate images for seen conditions, see Supplementary Fig. 6, with further details in Supplementary Note 1. It is apparent that the C-GAN outputs lag in image quality and contrast, as well as in the realistic and accurate depiction of microstructural features.

Virtual generation of microstructural images for unknown conditions utilising genAI

The C-DDPM generates images for both seen and unseen conditions, which are qualitatively indistinguishable from real FESEM-BSE micrographs. Further, the generated microstructural features obey the underlying physics for the evolution of IMC-thicknesses and Kirkendall pore areas. Ultimately, as indicated in Fig. 5, we generate microstructural images of unknown sample conditions in the investigated ageing time/Cu-impurity matrix. Real FESEM-BSE micrographs from all experimentally available conditions and their phase labels are shown and marked with 'SEM'. For the unknown conditions, images are generated utilising the C-DDPM and marked with 'genAI', as are their respective phase-labels. Again, the quality and contrast of the generated images for



unknown conditions are qualitatively indistinguishable from real FESEM-BSE micrographs and the virtually generated images blend into the matrix in Fig. 5 seamlessly. As before, the expected trends of IMC-layer growth with progressing ageing time and Kirkendall pore formation with increasing impurity content are qualitatively maintained in the images generated for unknown datapoints by the developed C-DDPM.

This result begs the question how well the virtually generated images quantitatively obey the underlying physical mechanisms of IMC-layer growth and Kirkendall pore area increase, i.e. how well the C-DDPM is able to learn these underlying physical mechanisms^{20,34}. This is analysed in the following section utilising the phase-labels exemplarily shown in Fig. 5 and Supplementary Fig. 4.

Fig. 4 | Model validation by generating images for seen and unseen conditions with the developed C-DDPM. **a** Physics-based C-DDPM validation workflow. Three microstructural images are generated for each experimentally available condition. The MS-SSIM is calculated in order to quantify the similarity between generated images and real FESEM-BSE micrographs, in terms of brightness, contrast and texture. Subsequently, the microstructural features, i.e. IMC-layers and Kirkendall pores, are qualitatively checked regarding their realism. In order to quantify how well the IMC-layer thicknesses and Kirkendall pore areas obey the underlying physical growth mechanisms, the microstructural features are manually labelled in both generated images and real FESEM-BSE micrographs. From the phase labels, microstructural features can be extracted and quantified. Based on the evolution of the depicted microstructural features, physics-based model validation is performed, for seen conditions and for unseen conditions. **b** Exemplary comparisons of real FESEM-BSE micrographs, marked 'SEM', with virtually generated ones, marked 'genAI' for seen datapoints and **c** unseen datapoints. Scalebars of 5 μm are valid for all images. The respective first rows show real FESEM-BSE micrographs for

b exemplary seen conditions with ECD1-0 h, PVD-100 h, ECD2-1000 h and ECD3-3000 h and **c** the unseen conditions with PVD-300 h and ECD1-750 h. The second rows show virtually generated images for the respective conditions from the first row. **d** Phase labels for the micrographs shown in **b** and **c**. Cu is labelled in blue, Cu_3Sn in yellow, Cu_6Sn_5 in purple, the SAC305 bulk in magenta, pores in green and Ag_3Sn -precipitates near the interface in salmon. Scalebar of 5 μm is valid for all labelled images. **e** Deviations of the phase labels for pore areas (green), Cu_6Sn_5 -thicknesses (purple) and Cu_3Sn -thicknesses (yellow) in generated images from the real mean values. Mean standard deviations of the respective features in real micrographs are shown as solid lines, whereas the deviations of generated images from the real mean values are shown as circles. For seen conditions, the mean deviations of all images that are generated for each of the four Cu-impurity contents are plotted, whereas for unseen conditions, the mean deviations of the three generated images for each of the two unseen conditions are plotted. The asterisk marks the deviation of the Cu_3Sn -layer thickness in the generated images for ECD1-750 h. Numerical values of all deviations are given in Supplementary Tables 3–5.

Quantitative model validation by evaluating physical quantities based on real and virtually generated microstructural images

The phase-labels of real FESEM-BSE micrographs, as well as those of generated images for seen, unseen and unknown datapoints from Fig. 5 and Supplementary Fig. 3 are further utilised for a quantitative assessment in the context of physical reasonability of the C-DDPM outputs. The physics-based validation workflow for unknown conditions is sketched in Fig. 6a. The phases in the generated microstructural images are manually labelled utilising ilastik⁷⁹, see 'Methods'. The microstructural features are extracted based on these labels and quantified. Thus, the microstructural evolution in real FESEM-BSE micrographs provides the underlying physical trend, and the model validation is performed based on how well the microstructural features depicted in generated images follow this trend^{20,34}.

Figure 6b, c shows the results for IMC-layer growth, i.e. cumulative Cu_3Sn - and Cu_6Sn_5 -growth, and Kirkendall pore area increase over ageing time at 150 °C for each Cu-impurity content. The PVD-samples are plotted in green, ECD1 in blue, ECD2 in purple and ECD3 in pink. The mean values of real FESEM-BSE micrographs are plotted as squares. Since the underlying physical mechanisms of both IMC- and pore-growth are of diffusional nature^{44,45,49,62,66,68,69,80,81}, these real values are fitted utilising square-root functions over ageing time, shown as dashed lines in Fig. 6b, c. The standard deviations of IMC-thicknesses and Kirkendall pore areas in the real FESEM-BSE micrographs are also fitted and illustrated as shaded areas around the square-root fits in Fig. 6b, c. For each datapoint in the ageing time / Cu-impurity matrix, three images are generated utilising the developed C-DDPM. The IMC-layer thicknesses and Kirkendall pore areas in these generated images are also plotted in Fig. 6b, c, wherein values for seen datapoints are shown as circles and values for unseen and unknown datapoints as triangles. Details about the analysis and data fitting are given in 'Methods'. The plots in Fig. 6b, c illustrate the square-root dependencies of IMC-layer growth and Kirkendall pore area increase, respectively, which are expected for diffusional processes. From Fig. 6b, it is evident that the IMC-layer growth rate increases slightly with increasing Cu-impurity content, while Fig. 6c shows that the Kirkendall pore area increases significantly with increasing Cu-impurity content. Crucially, it is shown that the generated images and their microstructural features quantitatively follow the square-root trends over time, regardless of whether they are generated for seen, unseen or unknown conditions. This validates the ability of the C-DDPM to learn the underlying physical mechanisms for IMC-layer growth and Kirkendall pore area increase from the real FESEM-BSE image data and to generate microstructural images accordingly. Note that the cumulative IMC-thicknesses, i.e. the sum of Cu_3Sn and Cu_6Sn_5 , are evaluated in Fig. 6b, because the ECD3-samples exhibit an irregularity for the individual Cu_3Sn - and Cu_6Sn_5 -thicknesses after being aged for 3000 h, as is qualitatively shown in Figs. 2 and 5 and quantitatively plotted in Supplementary Fig. 7. Therein, considering only real FESEM-BSE micrographs, the Cu_3Sn -thickness is decreased at 3000 h, compared to 750 h. Conversely, the Cu_6Sn_5 -thickness

increases disproportionately between these two timesteps. However, this discrepancy is removed when the sums of Cu_3Sn - and Cu_6Sn_5 -thicknesses are considered, which is shown in Fig. 6b, where square-root fitting is done for the cumulative IMC-layer thicknesses.

For the physics-based validation of the C-DDPM^{20,34}, the parabolic growth rates (k) are calculated for IMC layers and Kirkendall pore areas depending on the investigated Cu-impurities for real and generated images. For that, the cumulative IMC-thicknesses and pore areas are plotted over the square root of ageing time (\sqrt{t}), as shown in Fig. 6d, e, respectively. Again, plotting Cu_6Sn_5 - and Cu_3Sn -thicknesses separately over \sqrt{t} , leads to significant outliers for the ECD3 sample, see Supplementary Fig. 7a, b. It should be stressed that the generated images also consider this irregularity in Cu_6Sn_5 - and Cu_3Sn -growth, as also quantitatively plotted in Supplementary Fig. 7a, b. The consideration of this irregularity further underlines the ability of the C-DDPM to extract physical growth mechanisms from the real image data. Plotting the cumulative ($\text{Cu}_6\text{Sn}_5 + \text{Cu}_3\text{Sn}$) thicknesses and Kirkendall pore areas shows linear trends over \sqrt{t} for both real and generated data, see Fig. 6d, e. Hence, these properties are fitted linearly and the k 's are derived for each Cu-impurity content and for the real and generated images separately. Details about the fitting are given in 'Methods'. Figure 6d, e lists the respective k 's for cumulative IMC- and pore-growth for real and generated data, as well as the differences between them. As shown, the generated images utilising the C-DDPM follow the underlying physical mechanisms for IMC- and Kirkendall pore-growth very closely. The calculated k -values lie close to those from the real FESEM-BSE micrographs. The largest error for IMC-growth rates between real and generated images amounts to $-0.016 \mu\text{m}/\sqrt{\text{h}}$ for ECD3, which corresponds to -9.4% , see Fig. 6d, and the largest error for pore-growth is calculated as $0.007 \mu\text{m}^2/\sqrt{\text{h}}$, corresponding to 9.5% , as shown in Fig. 6e. Moreover, Fig. 6b–e shows that IMC- and Kirkendall pore-growth rates increase with increasing impurity content in the Cu metallisation. This is reflected in both real and generated data.

From the increase in the Kirkendall pore-growth rate with increasing Cu-impurity content, the changes in the Kirkendall pore formation enthalpy are estimated by a simplified ansatz. The calculations are described in 'Methods' and the results thereof are given in Table 1. Again, it is shown that the trends in the generated images follow the real ones and that the Kirkendall pore formation enthalpies decrease up to $\sim 10\%$ with increasing Cu-impurity content, compared to the PVD-sample, in both real and generated data. The estimated decrease in Kirkendall pore formation enthalpy with increasing Cu-impurity content holds true for both real and generated images. This, once again, highlights the C-DDPM's ability to generate microstructural images which consider the underlying physical driving forces, which are expressed in the real FESEM-BSE micrographs.

Discussion

Systematic and comprehensive studies of material degradation and root cause analyses are associated with labour-intensive and time-consuming

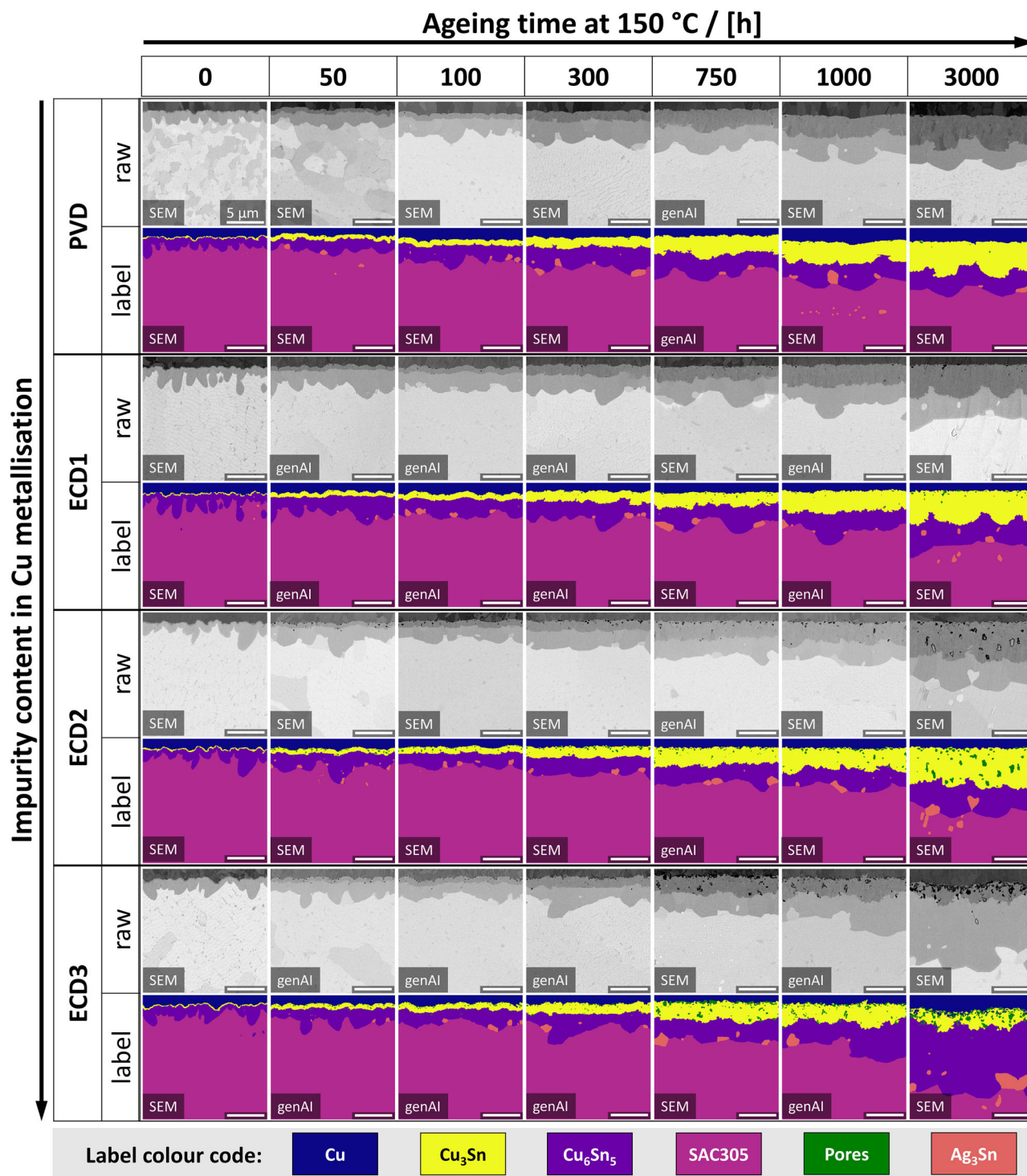
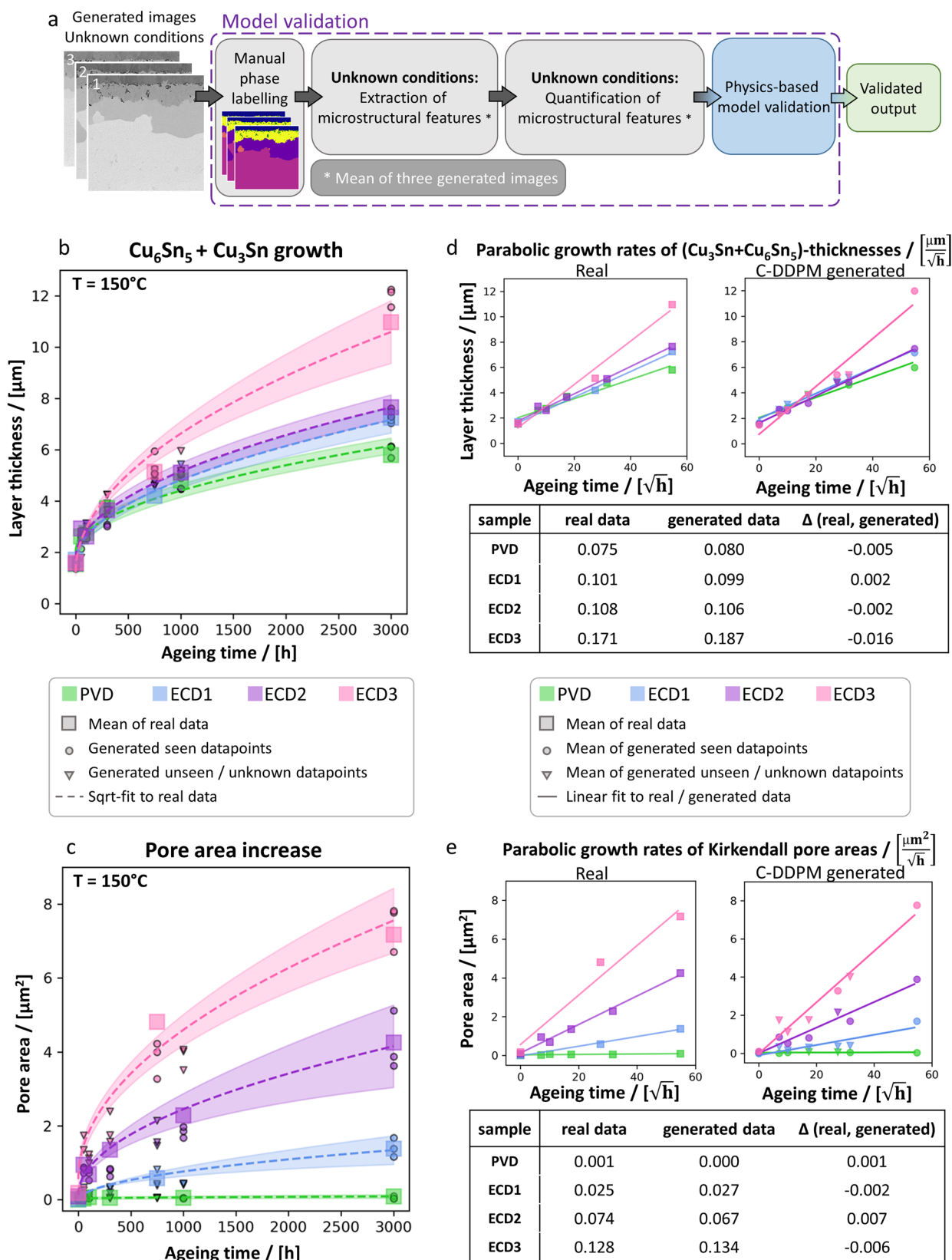


Fig. 5 | Complete sample matrix of real FESEM-BSE micrographs, filled up with virtually generated images of the Cu – SAC305 interfacial microstructures for the unknown conditions by the C-DDPM, as well as corresponding phase-labels. Sample matrix for the Cu-impurity contents and ageing times from Fig. 2. Unknown conditions are filled up utilising images generated by the C-DDPM and marked ‘genAI’. Exemplary raw images marked with ‘SEM’ indicate real FESEM-BSE

micrographs, whereas raw images marked with ‘genAI’ correspond to virtually generated data. For all images, their respective phase labels are also shown. In the phase labels, Cu is shown in blue, Cu₃Sn in yellow, Cu₆Sn₅ in purple, SAC305 in magenta, pores in green and Ag₃Sn-precipitates adjacent to the interface in salmon. Scalebars of 5 µm are valid for all images.

experimental work, especially when a variety of parameters are influential on the microstructural evolution, as the number of samples is significantly increased. Systematic sample fabrication and testing under controlled conditions alone take a substantial amount of time. Moreover, many

microstructural imaging methods, such as cross-sectional FESEM imaging, require careful sample preparation, which adds to the challenges facing experimentalists^{53,82–84}. In order to alleviate the heap of experimental work, this study shows the effectiveness and efficiency of a data-driven approach,



employing a C-DDPM for the generation of qualitatively realistic and quantitatively reasonable microstructural images of Cu–SAC305 interfaces in microelectronic devices for unknown sample conditions in the ageing time/Cu-impurity content matrix. A conditional data-driven genAI model is developed and validated based on how well the generated microstructural

images quantitatively obey the underlying physical mechanisms that drive the microstructural evolution. The results show that the developed C-DDPM is able to learn how the microstructures evolve according to the underlying physics and virtually generate microstructural images accordingly. Moreover, it is shown that genAI has the potential to reduce

Fig. 6 | Quantitative model precision analysis of IMC-layer growth and Kirkendall pore area increase for real and generated images, comprising seen, unseen and unknown datapoints. **a** Physics-based validation workflow for -DDPM generated microstructural images of unknown sample conditions. Three images are generated for each unknown sample condition. Since the C-DDPM generates images from random noise, the three generated images are not identical for each sample condition, resulting in some degree of variation. The microstructural features are manually labelled, extracted based on those labels, and quantified in terms of IMC-layer thickness and Kirkendall pore area. These quantities are further utilised for the C-DDPM validation. The physics-based model validation is elaborated in **b–e** for all sample conditions, i.e. seen, unseen and unknown. Therein, the microstructural evolution at Cu–SAC305 interfaces during isothermal ageing at 150 °C is

quantitatively analysed. The IMC-layer growths and Kirkendall pore area increases, dependent on the impurity content in the Cu metallisation, are plotted and the parabolic growth rates are determined and compared for real and generated images. PVD–Cu is plotted in green, ECD1–Cu in blue, ECD2–Cu in purple and ECD3–Cu in pink. **b, d** Cumulative ($\text{Cu}_6\text{Sn}_5 + \text{Cu}_3\text{Sn}$) layer growth. **c, e** Kirkendall pore area increases. **b, c** Mean values of the real images are shown as squares, square-root fits of these mean values as dashed lines and standard deviations as shaded areas versus the ageing time. The respective values of the three generated images for each sample condition are shown as circles (seen conditions) and triangles (unseen and unknown conditions). **d, e** Separate linear fitting of mean data from real and generated images and determination of parabolic growth rates versus the square root of ageing time.

Table 1 | Estimated pore formation enthalpy Q_K for the investigated Cu-impurity contents for real and generated data, respectively, as well as their decrease compared to Q_{PVD}

Estimated Kirkendall pore formation enthalpy				
sample	real data [$\frac{\text{kJ}}{\text{mol}}$]	generated data [$\frac{\text{kJ}}{\text{mol}}$]	Q_K/Q_{PVD} (real) [–]	Q_K/Q_{PVD} (generated) [–]
PVD	–106.83	–105.00	1.00	1.00
ECD1	–109.35	–113.07	1.02	1.07
ECD2	–117.78	–116.79	1.10	1.11
ECD3	–116.24	–119.30	1.09	1.13

experimental work for microstructural imaging significantly by training on a relatively small dataset of one real micrograph for each condition. This is schematically shown in Supplementary Fig. 1. However, the C-GAN, in contrast to the C-DDPM, fails to generate high-quality, diversified and realistic images, see Supplementary Fig. 6, because it relies on extensive hyperparameter tuning and big datasets for effective training^{18,20,23,24}. Moreover, the C-GAN is only able to generate images for seen conditions²³ and the quality of the generated images for those seen conditions is not comparable to those of C-DDPM in terms of generated artefacts, contrast and realism of the microstructural image, as shown in Supplementary Figs. 3 and 6. Hence, the C-DDPM is proven to be a promising tool for the generation of microstructural images of unknown conditions when only relatively few real micrographs are available.

In the following, we discuss the quality of the images generated by the developed C-DDPM, the model validation utilising quantitative physics-based microstructural feature analysis^{20,34}, as well as the implications for future scientific work. In general, the underlying physical mechanisms of the microstructural evolution at Cu–SAC305 interfaces during ageing are established^{45,46,62,68,69,80,85–87}. Hence, validation of the genAI model output can be done by extracting physical descriptors from the microstructural images and assessing how well the microstructural features in generated images obey the underlying physical mechanisms. Other possibilities comprise metrics like FID, which require large amounts of data⁸⁸ and cannot consider physical laws.

When examining Fig. 4b–c and Supplementary Figs. 2 and 3, it is illustrated that the microstructural images generated by the developed C-DDPM for seen conditions are qualitatively indistinguishable from the real FESEM–BSE micrographs. In terms of image clarity, quality and contrast, the generated virtual images closely imitate the real ones. This is also true for images that are generated for unseen and unknown conditions, as shown in Figs. 4b and 5, as well as Supplementary Fig. 2. The high image quality of the generated image data is also reflected by the calculated MS-SSIM, yielding a value of 0.79. It should be noted that the developed genAI algorithm is not limited to the virtual reconstruction of FESEM–BSE micrographs, but can be trained on any kind of experimental image data that depicts the microstructural features of interest, such as X-ray microscopy, transmission electron microscopy, or any other imaging technique. Since

the underlying driving forces of the microstructural evolution at Cu – SAC305 interfaces have been studied extensively and the physical mechanisms are rather well understood^{35,36,43–47,49,62,65,68,69,80,81,85–87}, the validation of the C-DDPM is performed by assessing how well the features of its generated images fit the physical expectations^{20,34}. This is done by quantitatively evaluating the IMC-thicknesses and Kirkendall pore areas, as well as their growth rates for the real and generated data. Note that the quantitative comparisons of real and generated images perform similarly well for seen and unseen conditions, when sufficient data about the specific impurity content and ageing time is available, as illustrated in Fig. 4 and Supplementary Tables 3–5. Moreover, the extracted microstructural features from the generated images for unknown datapoints fit well into the quantitative trends that are expected from the underlying physical mechanisms for diffusional growth^{44,45,49,62,66,68,69,76,77,80,81}.

The growth of both Cu_6Sn_5 - and Cu_3Sn -layers is expected due to the solid-state interdiffusion of Cu and Sn during isothermal ageing, as shown in previous experimental studies^{44,45,62,66,68,80,89}. Therein, Cu_3Sn grows at the Cu-rich side, whereas Cu_6Sn_5 is situated at the Sn-rich side^{44–46}. However, the experimental results in this study show that with increased Cu-impurity content and ageing time, Cu_3Sn -growth is somewhat hindered. This is illustrated by the fact that the Cu_3Sn -thickness decreases in the ECD3-sample between 750 h and 3000 h, which is depicted in Fig. 2, Supplementary Figs. 7 and 8. In return, the Cu_6Sn_5 -thickness increases disproportionately between those timesteps. Hence, it is assumed that the Cu_6Sn_5 -layer grows at the cost of the Cu_3Sn -layer if the Cu-impurity content and ageing time are elevated sufficiently. This may be caused by the increasing proportion of Kirkendall pores forming simultaneously during ageing due to the elevated Cu-impurity content^{49,66,69}, illustrated in Figs. 2 and 5, as well as Fig. 6c, e. Therein, the pore-fraction increases during ageing, slowly reducing the connected area between the Cu metallisation and the solder, which may disrupt Cu-diffusion and consequently, Cu_6Sn_5 continues to grow by consuming the Cu_3Sn -layer. Hence, the diffusional processes may continue overall, but with a limited supply of additional Cu from the metallisation. This is supported by the steady parabolic ($\text{Cu}_6\text{Sn}_5 + \text{Cu}_3\text{Sn}$)-growth shown in Fig. 6b. It is worth noting that the images generated by the C-DDPM also consider this effect, which is depicted in Fig. 5 and Supplementary Figs. 2 and 3. This, again, underlines the ability of the C-DDPM to extract the underlying physical mechanisms that affect the interfacial microstructure from real FESEM–BSE micrographs and generate microstructural images accordingly.

Hence, the C-DDPM generates microstructural images of specific sample conditions, which are both qualitatively indistinguishable from real FESEM–BSE micrographs and quantitatively follow the expected physical trends, i.e. parabolic growth due to interdiffusion of Cu, Sn, impurities and vacancies^{44,45,49,62,66,68,69,76,77,80,81}. To further validate the model's ability to learn the physical mechanisms affecting the microstructures, quantitative microstructural information extracted from both real and generated images, namely IMC-layer thicknesses and Kirkendall pore areas, is utilised for the estimation of physical quantities. Firstly, from quantitatively fitting the microstructural features depicted in both real and generated images, as depicted in Fig. 6b–e, the parabolic growth rates of cumulative IMC-

thicknesses and Kirkendall pore areas are extracted, which are presented in Fig. 6d–e, respectively. The increases in IMC-thickness and Kirkendall pore area and their accelerated growth rates with increasing Cu-impurity content are consistent with previous findings^{35,49,65,66,68,69}. Secondly, the decrease of Kirkendall pore formation enthalpy (Q_K) with increasing Cu-impurity content in the metallisation is estimated, as described in ‘Methods’. This estimated decrease in Q_K listed in Table 1, reflects the increasing Kirkendall pore area with increasing Cu-impurity content^{49,66,69}. It should be noted that here, only diffusional processes, extracted from the analysed image data, are considered for the estimation of Q_K and that there may be additional contributing factors involved. Nonetheless, the trend of decreasing Q_K with increasing Cu-impurity content for both real and generated images reiterates the viability of the images generated by the C-DDPM.

In summary, this study highlights the application of genAI for the image generation of unknown microstructural conditions in materials science, which may impact future approaches for microstructural imaging. The developed C-DDPM exhibits negligible hallucinations, and the ability of the model to extract significant cause variables from a relatively scarce number of seen conditions in its training data is validated. This has the potential to reduce experimental work significantly, as schematically shown in Supplementary Fig. 1. For future microstructural imaging analyses, a well-trained genAI model may limit the necessity for actual experimental work to the validation of the most promising or critical sample conditions. Similar interactions of AI and laboratory work are currently developing in the fields of biochemistry, e.g. the prediction of protein structures^{90–92}, and exploratory materials science, e.g. the prediction of high entropy alloy compositions^{93–95}. Hence, the findings from this study have great potential to advance failure analysis and material development since the developed method enables the holistic microstructural imaging of critical conditions with high efficiency in context to microstructural evolution and material degradation, also when only few experimental sample conditions are available.

Methods

Materials and sample production

The investigated samples were prepared on 300 mm Si wafers using industrial manufacturing processes. The ECD-Cu metallisations are deposited at room temperature from a liquid electrolyte, utilising the current densities listed in Supplementary Table 1. The investigated PVD-Cu metallisations are grown at room temperature using physical vapour deposition. Both ECD-Cu and PVD-Cu type samples have a final Cu thickness of 10 μm .

The investigated solder balls are made from the Sn–3.0 wt.% Ag–0.5 wt.% Cu (SAC305) solder alloy, which is reflowed at a peak temperature of 240 °C and with a mean heating rate of 44 °C/min in inert N_2 atmosphere, followed by rapid air cooling to 90 °C with a mean cooling rate of 107 °C/min and ambient air cooling to room temperature. Subsequently, the PVD- and ECD2-samples are aged for 0, 50, 100, 300, 1000 and 3000 h at 150 °C in ambient atmosphere, whereas the ECD1- and ECD3-samples are aged for 0, 750 and 3000 h at the same conditions. Note that the ageing test is carefully chosen with respect to the eutectic temperature of SAC305, which is only 217 °C⁹⁶. Therefore, a drastic increase of the ageing temperature to further speed up the microstructural change would risk changes in the ageing mechanisms.

3D X-ray tomography

The exemplary 3D X-ray tomography, shown in Fig. 1a, is done with a GE Phoenix Nanotom M (research edition) with a cone-beam, 110 kV acceleration voltage, 120 μA X-ray tube current and without filter. By utilising a cone-beam, the achievable spatial resolution is dependent on the lateral sample size ($\sim 5 \times 5 \text{ mm}^2$). This results in a voxel size of $2.35 \times 2.35 \times 2.35 \mu\text{m}^3$. Due to the various X-ray attenuation by the different materials in the device, solder balls, Cu metallisations, as well as flux bubbles within the solder balls, are distinguishable due to their various grey values. The visualisation in Fig. 1a is done with Avizo.

Sample preparation and FESEM imaging

A 3D Micromac microPREP PRO femtosecond laser with a laser power of 300 mW is used to pre-prepare the cross-sections for FESEM. The final cross-sections for FESEM-BSE imaging are prepared with a Hitachi IM4000+ ion milling system. The accelerating voltage for ion slicing is set to 6 kV and the swing angle to 30°. The BSE micrographs are acquired with a Zeiss 450 Gemini FESEM utilising an acceleration voltage of 5 kV, sample currents of 3 nA and a 1000 X-magnification. The EDX-mappings are done on the same Zeiss system utilising an Oxford Ultim Extreme EDX-detector.

C-DDPM model and image generation

For the virtual generation of microstructural images for specific sample conditions, we utilise a conditional denoised diffusion probabilistic model (C-DDPM), see Fig. 3. Solely FESEM-BSE micrographs are utilised to train the C-DDPM. The experimentally available dataset in this study includes 18 actual FESEM-BSE micrographs from ageing times 0 h, 50 h, 100 h, 300 h, 750 h, 1000 h, and 3000 h and Cu impurity contents of 0, 30, 60, and 120. These are the 18 different experimentally available sample conditions illustrated in Fig. 2. For the virtual generation of the microstructural image data, we distinguish between three types of conditions: seen, unseen and unknown. We utilise 1080 microstructural images for the training of the C-DDPM. The FESEM-BSE micrographs, one image for each seen condition, are cropped utilising a sliding-window approach. The window size is set to 450×450 pixels² with a horizontal overlap of 400 pixels. The resulting image snippets show a field of view of $16.75 \times 16.75 \mu\text{m}^2$ and are then resized to 512×512 pixels² for the training of the C-DDPM and C-GAN. Data augmentation is performed by using a vertical flip, since the microstructure images are variant to rotation, and they are normalised to the intensity of $[-1, 1]$. We calculate the silhouette value utilising scikit-learn 1.2.1 to gain a quality measure about clustering in the training data, to ensure data diversity despite the image overlap of the FESEM-BSE snippets. The silhouette value can assume values from -1 to $+1$. For our training data, the silhouette value is calculated as 0.29, indicating high data diversity⁹⁷. For the evaluation of the model prediction ability, two unseen conditions are set aside during model training. We consider a 10:90 validation data split. The C-DDPM model is trained for 400 epochs with a batch size of 2 on a single HP ProLiant A40 GPU Gen10 server in Python 3.11 using the Pytorch 2.1 library, which is the dataset passes through an algorithm 400 times. The time step of noise production is set to 1000, and the start and end points of the variance scheduler β are 0.0001 and 0.02, respectively. The learning rate of Adam optimiser is set to 0.0003. We generate with the trained model three images for each datapoint. after the denoising process.

The model is briefly introduced here, according to^{22–24}. The diffusion process gradually adds Gaussian noise to a clean image x_0 over T time steps using a predefined variance schedule β_t . The diffusion equation is given as:

$$q(x_t|x_{t-1}) = \mathcal{N}(x_t; \sqrt{1 - \beta_t}x_{t-1}, \beta_t\mathbf{I}), \quad (1)$$

where β_t controls the noise level at each timestep t , \mathbf{I} is the identity matrix, and T is total step number. Using the re-parameterisation trick, x_t can be sampled directly at any timestep:

$$x_t = \sqrt{\bar{\alpha}_t}x_0 + \sqrt{1 - \bar{\alpha}_t}\epsilon \quad (2)$$

here $\bar{\alpha}_t = \prod_{s=1}^t (1 - \beta_s)$ is the cumulative product of noise scaling factors, and $\epsilon \sim \mathcal{N}(0, \mathbf{I})$ is standard Gaussian noise. The diffusion process is fixed and does not involve learnable parameters.

The denoising procedure aims to recover the original image x_0 from noisy images x_T, x_{T-1}, \dots, x_1 . It is parameterised by a convolutional neural network architecture with attention gates (U-Net)⁷⁴, and modelled as:

$$\mathcal{P}_\theta(x_{t-1}|x_t, f) = \mathcal{N}(\mu_\theta(x_t, t, f), \sigma_t^2\mathbf{I}) \quad (3)$$

where f denotes the conditioning information and $\mu_\theta(x_t, t, f)$ is the mean parameterisation, which is predicted by a U-Net. A variance term σ_t^2 is fixed

to a certain schedule. The mean prediction is typically parameterised as:

$$\mu_{\theta}(x_t, t, f) = \frac{1}{\sqrt{\alpha_t}}(x_t - \frac{\beta_t}{\sqrt{1 - \alpha_t}}\epsilon_{\theta}(x_t, t, f)) \quad (4)$$

Where $\epsilon_{\theta}(x_t, t, f)$ predicts the noise added to x_0 .

The training objective is to minimise the difference between the true noise (ϵ) and the predicted noise $\epsilon_{\theta}(x_t, t, f)$ at each timestep t based on condition f using a simplified loss function:

$$L_{\theta} = \mathbb{E}_{x_0, t, f, \epsilon} [\|\epsilon - \epsilon_{\theta}(x_t = \sqrt{\alpha_t}x_0 + \sqrt{1 - \alpha_t}\epsilon, t, f)\|^2] \quad (5)$$

This loss function trains the model to predict noise accurately at each timestep while respecting conditional f . The expectation \mathbb{E} ensures that the model generalises across different timesteps, noise levels, and conditions.

The encoding and decoding paths of the implemented attention U-Net model are asymmetric and mirrored, with six layers each. The encoding path consists of six blocks of max-pooling, four convolutional layers, group normalisation, and a Gaussian Error Linear Unit (GELU) activation function, see Fig. 3. Ahead of max-pooling in the first layer, there are two convolutional layers. The bottleneck consists of six convolutional layers. The self-attention mechanism with four heads is applied from the third to the sixth down-sampling layers to address long-range and multi-level dependencies across image regions. The decoding path is similar to the encoder, with six blocks of bi-linear up-sampling and four convolutional layers followed by group normalisation and GELU activation functions, and the final layer is a 1×1 convolution. The decoding path concatenates data with skip connections to prevent spatial information loss and alleviate the vanishing gradient problem. There are self-attention layers similar to the encoding path after up-sampling of the sixth to third layers. During denoising, the model is conditioned on the timestep using the sinusoidal positional embedding, added to each down-sampling and up-sampling layer. To make it class-conditional, similar to the timestep at each down- and up-sampling layer, the embedding vectors corresponding to Cu-impurity and ageing time are linearly embedded into separate tensors of the same size as the corresponding layer's spatial dimension and concatenated with related feature maps. The Adam optimizer and mean squared error (MSE) loss function are used for training, while the exponential moving average technique (EMA) calculates the exponentially weighted average of the current and updated model parameters at each optimisation step to stabilise the optimisation process. For the training and validation of the C-DDPM, the dataset shown in Fig. 2 is utilised.

The U-Net is implemented as the backbone of the C-DDPM due to its hierarchical feature extraction, its skip connections, and its empirical performance. It processes images through layers, capturing features at multiple scales, and preserves spatial information. U-Nets are well-suited for handling noise in the denoising process and can be modified to include additional features like attention mechanisms⁷⁴. These traits make U-Nets valuable components in generating high-quality images. This allows the virtual reconstruction of original images by gradually removing noise.

Validation of generated images by the C-DDPM in seen and unseen datapoints, as well as assessment of reasonability for generated images in unknown datapoints

The developed C-DDPM generates microstructural images for specific sample conditions from random noise, within the second Markov chain. Since the denoising begins with random noise, and a stochastic approach is utilised due to the Markov chain, those images will not be identical. Therefore, in order to gain more statistical insight into the model outputs, three images are generated for each condition. For the extraction of the microstructural features, like IMC-layer thicknesses and Kirkendall pore areas, the FESEM-BSE micrographs, as well as the generated microstructural images, are labelled using ilastik 7.1.0⁷⁹. We apply the embedded feature suggestion tool for pre-segmentation and subsequently manually refine the labels to maximise the label accuracy. For each of these labelled

images, the mean Cu_6Sn_5 - and Cu_3Sn -thicknesses are calculated by counting the number of pixels of the respective phase, dividing by the image width and multiplying with the pixel size. The pore area is also calculated by counting the associated pixels and multiplying with the pixel size. Subsequently, an average is taken from the three images that are generated for each sample condition. The deviations of the respective features in the generated images from the real FESEM-BSE micrographs are evaluated separately for each datapoint, for both seen and unseen data. The deviations are calculated by dividing the differences between the mean values in real and generated images by the mean of the respective real values. For the evaluation of structural similarity between real and generated images, the MS-SSIM is calculated utilising TensorFlow 2.6.0. The calculated value of 0.79 indicates high similarity between the images in terms of brightness, contrast and texture. In order to further scrutinise the microstructural morphologies in generated images, the Cu_6Sn_5 -SAC305 interface curvatures are exemplarily calculated for PVD-Cu metallisation after isothermal ageing for 0, 100, 300, 1000 and 3000 h and compared to real interface curvatures of the respective conditions, see Supplementary Fig. 5. Specifically, the line-lengths of the interfaces are calculated, as they directly correlate with the interface curvatures. As shown, the C-DDPM is also able to realistically depict this property, as the maximum deviation amounts to 8%.

For the physics-based model validation, the manually labelled phases are quantified for each Cu-impurity content and plotted over isothermal ageing time. Python 3.8.13 and Numpy 1.22.3 are used for calculating and plotting the evolution of the microstructural features over time. Square-root fitting on real data is done with SciPy 1.7.3 and plotted, along with the standard deviation in the real images. The values for generated images are also added to the plots to visualise their deviations from the real data with Matplotlib 3.5.1. For the generated images, seen conditions are plotted as circles, unseen and unknown conditions as triangles. Note that 'unknown' conditions are sample conditions, which are experimentally not available.

Calculation of parabolic growth rates

The calculations of the parabolic growth rates of both IMC layers and Kirkendall pores are based on the labelled images and their aforementioned quantification. Again, Python 3.8.13 and Numpy 1.22.3 are used for calculating and plotting the evolution of the microstructural features and SciPy 1.7.3 for data-fitting, only this time, linear fitting is applied over \sqrt{t} . From the slopes of these linear fits, the respective parabolic growth rates are determined.

Estimation of Kirkendall pore formation enthalpies

The estimation of Kirkendall pore formation enthalpy is based on the pore area increase observed over ageing time and increasing Cu-impurity content. Numerical values for the calculations are roughly estimated from the experimental data in this study and from literature. Hence, the results and discussion in this context are only done comparatively for the investigated Cu-impurity contents and numerical values should not be taken at their face values but only the trends should be considered.

The increase in Kirkendall pore area with increasing Cu-impurity content is shown in Fig. 6b, d. In order to estimate the decrease of the pore formation enthalpy, the vacancy diffusion coefficients (D_v) are assessed from the pore-area increase over ageing time. For simplicity, D_v is calculated as

$$D_v / \left[\frac{\text{m}^2}{\text{s}} \right] = \frac{\text{pore-area}}{t} \quad (6)$$

wherein the mean D_v value of the various ageing timesteps is evaluated for each sample. Subsequently, the Kirkendall pore formation enthalpies (Q_K /[kJ/mol]) are estimated:

$$Q_K / \left[\frac{\text{kJ}}{\text{mol}} \right] = -R \cdot T \cdot \ln \left(\frac{D_v}{D_0} \right) / 1000 \quad (7)$$

where $R/[kJ/mol]$ denotes the ideal gas constant and $T/[K]$ the ageing temperature. Due to lacking literature on D_0 for vacancy diffusion in Cu_3Sn , the intrinsic diffusion coefficient of Cu_3Sn ($D_{Cu_3Sn} = 5.48 \times 10^{-9} \text{ m}^2/\text{s}^{98,99}$) is inserted instead. The results of this estimation are shown in Table 1. It should be stressed that D_0 and D_v are only roughly estimated in their numerical values, nonetheless, both values are determined in the same way for all samples. Hence, the ratio of Q_K of each ECD deposition current density and the PVD-deposited Cu-sample (Q_{PVD}) is calculated for both real and generated data, respectively.

Data availability

Data is provided within the manuscript or supplementary information files. Further data if necessary is available from the corresponding author upon request.

Code availability

All code that supports the findings of this study is available from the corresponding author upon reasonable request.

Received: 12 February 2025; Accepted: 28 April 2025;

Published online: 17 May 2025

References

- Zhao, Y. & Liu, G. How do teachers face educational changes in artificial intelligence era? *Adv. Social Sci. Educ. Human. Res.* 47–50 (2018).
- Fullan, M., Azorin, C., Harris, A. & Jones, M. Artificial intelligence and school leadership: challenges, opportunities and implications. *Sch. Leadersh. Manag.* **44**, 339–346 (2024).
- Kim, N. J. & Kim, M. K. Teachers' perceptions of using an artificial intelligence-based educational tool for scientific writing. *Front. Educ.* **7**, 755914 (2022).
- Zhang, P. & Kamel Boulos, M. N. Generative AI in medicine and healthcare: promises, opportunities and challenges. *Future Internet* **15**, 286 (2023).
- Paladugu, P. S. et al. Generative adversarial networks in medicine: important considerations for this emerging innovation in artificial intelligence. *Ann. Biomed. Eng.* **51**, 2130–2142 (2023).
- Chen, Y. & Esmaeilzadeh, P. Generative AI in medical practice: in-depth exploration of privacy and security challenges. *J. Med. Internet Res.* **26**, e53008 (2024).
- Karimzadeh, M. et al. Deep generative AI models analyzing circulating orphan non-coding RNAs enable detection of early-stage lung cancer. *Nat. Commun.* **15**, 10090 (2024).
- Lovato, J., Witte Zimmerman, J., Smith, I., Dodds, P. & Karson, J. L. Foregrounding artist opinions: a survey study on transparency, ownership, and fairness in AI generative Art. In *Proc. of the 7th AAAI/ACM Conference on AI, Ethics, and Society*, 905–916 (The AAAI Press, Washington, DC, USA, 2024).
- Zhou, E. & Lee, D. Generative artificial intelligence, human creativity, and art. *PNAS Nexus* **3**, 1–8 (2024).
- Fitria, T. N. Artificial intelligence (AI) technology in OpenAI ChatGPT application: a review of ChatGPT in writing english essay. *J. Eng. Lang. Teach.* **12**, 44–58 (2023).
- Borji, A. Generated faces in the wild: quantitative comparison of stable diffusion, midjourney and DALL-E 2. *arXiv:2210.00586* (2022).
- Vaswani, A. et al. Attention is All you Need. In *Proc. Advances in Neural Information Processing Systems*, edited by I. Guyon, et al. (Curran Associates, Inc., 2017).
- Radford, A., Narasimhan, K., Salimans, T. & Sutskever, I. Improving language understanding by generative pre-training (2018).
- Radford, A. et al. *Language Models are Unsupervised Multitask Learners* (2019).
- Boiko, D. A., MacKnight, R., Kline, B. & Gomes, G. Autonomous chemical research with large language models. *Nature* **624**, 570–578 (2023).
- Liu, N. et al. Harnessing large language models for data-scarce learning of polymer properties. *Nat. Comput. Sci.* **5**, 245–254 (2025).
- Demszy, D. et al. Using large language models in psychology. *Nat. Rev. Psychol.* **14**, 1279317 (2023).
- Lyu, X. & Ren, X. Microstructure reconstruction of 2D/3D random materials via diffusion-based deep generative models. *Sci. Rep.* **14**, 5041 (2024).
- Goodfellow, I. J. et al. *Generative Adversarial Nets*. Advances in neural information processing systems, **27** (2014).
- Wijaya, A., Wagner, J., Sartory, B. & Brunner, R. Analyzing microstructure relationships in porous copper using a multi-method machine learning-based approach. *Commun. Mater.* **5**, 59 (2024).
- Cao, H. et al. A survey on generative diffusion models. *IEEE Trans. Knowl. Data Eng.* **36**, 2814–2830 (2024).
- Ho, J., Jain, A. & Abbeel, P. Denoising diffusion probabilistic models. Advances in neural information processing systems, **33**, 6840–6851 (2020).
- Azqadan, E., Jahed, H. & Arami, A. Predictive microstructure image generation using denoising diffusion probabilistic models. *Acta Mater.* **261**, 119406 (2023).
- Khader, F. et al. Denoising diffusion probabilistic models for 3D medical image generation. *Sci. Rep.* **13**, 7303 (2023).
- Amit, T., Shaharabany, T., Nachmani, E. & Wolf, L. SegDiff: image segmentation with diffusion probabilistic models. *arXiv:2112.00390* (2021).
- Li, X. et al. Diffusion-Im improves controllable text generation. Advances in neural information processing systems, **35**, 4328–4343 (2022).
- Yang, L. et al. Diffusion models: a comprehensive survey of methods and applications. *ACM Comput. Surv.* **56**, 1–39 (2024).
- Xie, T., Fu, X., Ganea, O.-E., Barzilay, R. & Jaakkola, T. Crystal diffusion variational autoencoder for periodic material generation. *arXiv:2110.06197* (2021).
- Xie, Y. & Li, Q. Measurement-conditioned denoising diffusion probabilistic model for under-sampled medical image reconstruction. International Conference on Medical Image Computing and Computer-Assisted Intervention, 655–664 (2022).
- GM, H., Gourisaria, M. K., Pandey, M. & Rautaray, S. S. A comprehensive survey and analysis of generative models in machine learning. *Comput. Sci. Rev.* **38**, 100285 (2020).
- Aithal, S. K., Maini, P., Lipton, Z. C. & Kolter, J. Z. Understanding hallucinations in diffusion models through mode interpolation. *arXiv:2406.09358* (2024).
- Sun, Y., Sheng, D., Zhou, Z. & Wu, Y. AI hallucination: towards a comprehensive classification of distorted information in artificial intelligence-generated content. *Humanit. Soc. Sci. Commun.* **11**, 1278 (2024).
- Farquhar, S., Kossen, J., Kuhn, L. & Gal, Y. Detecting hallucinations in large language models using semantic entropy. *Nature* **630**, 625–630 (2024).
- Bostanabad, R. et al. Computational microstructure characterization and reconstruction: Review of the state-of-the-art techniques. *Prog. Mater. Sci.* **95**, 1–41 (2018).
- Pal, M. K. & Bajaj, V. Nucleation and location of kirkendall voids at the tin-based solder/copper joint: a review. *Adv. Eng. Mater.* **25**, 2300671 (2023).
- Takenaka, T., Kano, S., Kajihara, M., Kurokawa, N. & Sakamoto, K. Growth behavior of compound layers in Sn/Cu/Sn diffusion couples during annealing at 433–473. *K. Mater. Sci. Eng. A* **396**, 115–123 (2005).
- Cui, C. et al. Correlative, ML-based and non-destructive 3D-analysis of intergranular fatigue cracking in SAC305-Bi solder balls. *npj Mater. Degrad.* **8**, 40 (2024).
- Paulachan, P., Siegert, J., Wiesler, I. & Brunner, R. An end-to-end convolutional neural network for automated failure localisation and characterisation of 3D interconnects. *Sci. Rep.* **13**, 9376 (2023).

39. Furat, O. et al. Machine learning techniques for the segmentation of tomographic image data of functional materials. *Front. Mater.* **6**, 452734 (2019).
40. Pahwa, R. et al. Deep learning analysis of 3D X-ray images for automated object detection and attribute measurement of buried package features. In *Proc. Electronic Packaging Technology Conference*, 221–227 (2020).
41. Hsu, P.-N. et al. Artificial intelligence deep learning for 3D IC reliability prediction. *Sci. Rep.* **12**, 6711 (2022).
42. Chantaramanee, S. & Sungkhaphaitoon, P. Influence of bismuth on microstructure, thermal properties, mechanical performance, and interfacial behavior of SAC305-xBi/Cu solder joints. *Trans. Nonferrous Met. Soc. China* **31**, 1397–1410 (2021).
43. Deshpande, A., Jiang, Q. & Dasgupta, A. Effect of microscale heterogeneities and stress state on the mechanical behavior of solder joints. In *Proc. 2020 19th IEEE Intersociety Conference on Thermal and Thermomechanical Phenomena in Electronic Systems (ITherm)*, 1024–1028 (IEEE, 2020).
44. Ho, C. E. et al. IMC microstructure modification and mechanical reinforcement of Sn–Ag–Cu/Cu microelectronic joints through an advanced surface finish technique. *J. Mater. Res. Technol.* **11**, 1895–1910 (2021).
45. Hodúlová, E., Palcut, M., Lechovič, E., Šimeková, B. & Ulrich, K. Kinetics of intermetallic phase formation at the interface of Sn–Ag–Cu–X (X=Bi, In) solders with Cu substrate. *J. Alloy. Compd.* **509**, 7052–7059 (2011).
46. Hsu, W.-N. & Ouyang, F.-Y. Effect of Ag₃Sn: effective suppression of thermomigration-induced Cu dissolution in micro-scale Pb-free interconnects. *Mater. Chem. Phys.* **165**, 66–71 (2015).
47. Hu, S.-H. et al. Effects of bismuth additions on mechanical property and microstructure of SAC-Bi solder joint under current stressing. *Microelectron. Reliab.* **117**, 114041 (2021).
48. Lennon, A., Colwell, J. & Rodbell, K. P. Challenges facing copper-plated metallisation for silicon photovoltaics: Insights from integrated circuit technology development. *Prog. Photovolt.* **27**, 67–97 (2019).
49. Ross, G. et al. XRD and ToF-SIMS study of intermetallic void formation in Cu–Sn micro-connects. *Microelectron. Reliab.* **76–77**, 390–394 (2017).
50. Olofinjana, A., Haque, R., Mathir, M. & Voo, N. Studies of the solidification characteristics in Sn–Ag–Cu–Bi solder alloys. *Procedia Manuf.* **30**, 596–603 (2019).
51. Yang, C., Liu, Y., Nishikawa, H. & Lin, S. Reducing anisotropy of rhombohedral Bi-rich phase for high-performance Ag–alloyed Sn–Bi low-temperature solders. *J. Mater. Res. Technol.* **30**, 16–24 (2024).
52. Ben Romdhane, E., Guédon-Gracia, A., Pin, S., Roumanille, P. & Frémont, H. Impact of crystalline orientation of lead-free solder joints on thermomechanical response and reliability of ball grid array components. *Microelectron. Reliab.* **114**, 113812 (2020).
53. Henderson, D. W. et al. The microstructure of Sn in near-eutectic Sn–Ag–Cu alloy solder joints and its role in thermomechanical fatigue. *J. Mater. Res.* **19**, 1608–1612 (2004).
54. Korhonen, T.-M. K., Lehman, L. P., Korhonen, M. A. & Henderson, D. W. Isothermal fatigue behavior of the near-eutectic Sn–Ag–Cu alloy between –25 °C and 125 °C. *J. Elec. Mater.* **36**, 173–178 (2007).
55. Zachariasz, P. et al. Mössbauer studies of $\beta \rightarrow \alpha$ phase transition in Sn-rich solder alloys. *Microelectron. Reliab.* **82**, 165–170 (2018).
56. Dudek, M. A. et al. Three-dimensional (3D) visualization of reflow porosity and modeling of deformation in Pb-free solder joints. *Mater. Charact.* **61**, 433–439 (2010).
57. Kim, J. et al. Oxidation and repeated-bending properties of Sn-based solder joints after highly accelerated stress testing (HAST). *Electron. Mater. Lett.* **14**, 678–688 (2018).
58. Lehman, L. P., Xing, Y., Bieler, T. R. & Cotts, E. J. Cyclic twin nucleation in tin-based solder alloys. *Acta Mater.* **58**, 3546–3556 (2010).
59. Huang, M. L. & Wang, L. Effects of Cu, Bi, and In on microstructure and tensile properties of Sn–Ag–X(Cu, Bi, In) solders. *Met. Mat. Trans. A* **36**, 1439–1446 (2005).
60. Deshpande, A., Kaeser, H. & Dasgupta, A. Effect of stress state on fatigue characterization of SAC305 solder joints. In *Proc. 10th International Conference 2019*, 1–3. (IEEE, 2019).
61. Depiver, J. A., Mallik, S. & Amalu, E. H. Effective solder for improved thermo-mechanical reliability of solder joints in a ball grid array (BGA) soldered on printed circuit board (PCB). *J. Elec. Mater.* **50**, 263–282 (2021).
62. Li, Q. & Chan, Y. C. Growth kinetics of the Cu₃Sn phase and void formation of sub-micrometre solder layers in Sn–Cu binary and Cu–Sn–Cu sandwich structures. *J. Alloy. Compd.* **567**, 47–53 (2013).
63. Tsao, L. C. Evolution of nano-Ag₃Sn particle formation on Cu–Sn intermetallic compounds of Sn_{3.5}Ag_{0.5}Cu composite solder/Cu during soldering. *J. Alloy. Compd.* **509**, 2326–2333 (2011).
64. Chung, C. K., Duh, J.-G. & Kao, C. R. Direct evidence for a Cu-enriched region at the boundary between Cu₆Sn₅ and Cu₃Sn during Cu/Sn reaction. *Scr. Mater.* **63**, 258–260 (2010).
65. Panchenko, I. et al. Degradation of Cu₆Sn₅ intermetallic compound by pore formation in solid–liquid interdiffusion Cu/Sn microbump interconnects. *Microelectron. Eng.* **117**, 26–34 (2014).
66. Zhou, S., Zhang, Y.-B., Gao, L.-Y., Li, Z. & Liu, Z.-Q. The self-healing of Kirkendall voids on the interface between Sn and (1 1 1) oriented nanotwinned Cu under thermal aging. *Appl. Surf. Sci.* **588**, 152900 (2022).
67. Kelly, M. B., Niverty, S. & Chawla, N. Four dimensional (4D) microstructural evolution of Cu₆Sn₅ intermetallic and voids under electromigration in bi-crystal pure Sn solder joints. *Acta Mater.* **189**, 118–128 (2020).
68. Lin, K. et al. Growth behavior and formation mechanism of porous Cu₃Sn in Cu/Sn solder system. *Mater. Charact.* **178**, 111271 (2021).
69. Yu, J. & Kim, J. Y. Effects of residual S on Kirkendall void formation at Cu/Sn–3.5Ag solder joints. *Acta Mater.* **56**, 5514–5523 (2008).
70. Salakhutdinov, R. Learning deep generative models. *Annu. Rev. Stat. Appl.* **2**, 361–385 (2015).
71. Kingma, D. P., Rezende, D. J., Mohamed, S. & Welling, M. Semi-supervised learning with deep generative models. *Advances in neural information processing systems*, **27** (2014).
72. Akers, S. et al. Rapid and flexible segmentation of electron microscopy data using few-shot machine learning. *npj Comput. Mater.* **7**, 187 (2021).
73. Bihani, A. et al. MudrockNet: Semantic segmentation of mudrock SEM images through deep learning. *Comput. Geosci.* **158**, 104952 (2022).
74. Chamasemani, F. F., Lenzhofer, F. & Brunner, R. Deep learning revealed statistics of the MgO particles dissolution rate in a CaO–Al₂O₃–SiO₂–MgO slag. *Sci. Rep.* **14**, 21279 (2024).
75. Wang, Z., Simoncelli, E. P. & Bovik, A. C. Multiscale structural similarity for image quality assessment. In *Proc. The Thirty-Seventh Asilomar Conference on Signals, Systems & Computers*, 1398–1402 (IEEE, 2003).
76. Gottstein, G. *Physikalische Grundlagen der Materialkunde*. 3rd ed (Springer, 2007).
77. Haasen, P. *Physikalische Metallkunde*. 3rd ed (Springer, 1994).
78. Liu, P. S., Li, T. F. & Fu, C. Relationship between electrical resistivity and porosity for porous metals. *Mater. Sci. Eng. A* **268**, 208–215 (1999).
79. Berg, S. et al. Ilastik: interactive machine learning for (bio)image analysis. *Nat. Methods* **16**, 1226–1232 (2019).
80. He, A. & Ivey, D. G. Microstructural study of Sn films electrodeposited on Cu substrates: Sn whiskers and Cu₆Sn₅ precipitates. *J. Mater. Sci.* **50**, 2944–2959 (2015).
81. Schaefer, M., Fournelle, R. A. & Liang, J. Theory for intermetallic phase growth between Cu and liquid Sn–Pb solder based on grain boundary diffusion control. *J. Elec. Mater.* **27**, 1167–1176 (1998).
82. Cen, X. & van Benthem, K. Ion beam heating of kinetically constrained nanomaterials. *Ultramicroscopy* **186**, 30–34 (2018).

83. Kaira, C. S., Singh, S. S., Kirubanandham, A. & Chawla, N. Microscale deformation behavior of bicrystal boundaries in pure tin (Sn) using micropillar compression. *Acta Mater.* **120**, 56–67 (2016).
84. Cui, C. et al. Effective preparation of low-melting solder materials for atom probe tomography. *Sci. Rep.* **14**, 29475 (2024).
85. Yuan, Y., Guan, Y., Li, D. & Moelans, N. Investigation of diffusion behavior in Cu–Sn solid state diffusion couples. *J. Alloy. Compd.* **661**, 282–293 (2016).
86. Mazullah et al. Thermal aging impact on microstructure, creep and corrosion behavior of lead-free solder alloy (SAC387) use in electronics. *Microelectron. Reliab.* **122**, 114180 (2021).
87. Kumar, S., Handwerker, C. A. & Dayananda, M. A. Intrinsic and Interdiffusion in Cu–Sn System. *J. Phase Equilib. Diffus.* **32**, 309–319 (2011).
88. Jayasumana, S. et al. Rethinking FID: towards a better evaluation metric for image generation. Proceedings of the IEEE/CVF Conference on Computer Vision and Pattern Recognition, 9307–9315 (2024).
89. Hektor, J., Micha, J.-S., Hall, S. A., Iyengar, S. & Ristinmaa, M. Long term evolution of microstructure and stress around tin whiskers investigated using scanning Laue microdiffraction. *Acta Mater.* **168**, 210–221 (2019).
90. AlQuraishi, M. Machine learning in protein structure prediction. *Curr. Opin. Chem. Biol.* **65**, 1–8 (2021).
91. Torrisi, M., Pollastri, G. & Le, Q. Deep learning methods in protein structure prediction. *Comput. Struct. Biotechnol. J.* **18**, 1301–1310 (2020).
92. King, R. & Sternberg, M. Machine learning approach for the prediction of protein secondary structure. *J. Mol. Biol.* **216**, 441–457 (1990).
93. Wen, C. et al. Machine learning assisted design of high entropy alloys with desired property. *Acta Mater.* **170**, 109–117 (2019).
94. Liu, X., Zhang, J. & Pei, Z. Machine learning for high-entropy alloys: progress, challenges and opportunities. *Prog. Mater. Sci.* **131**, 101018 (2023).
95. Huang, W., Martin, P. & Zhuang, H. L. Machine-learning phase prediction of high-entropy alloys. *Acta Mater.* **169**, 225–236 (2019).
96. Cai, C., Xu, J., Wang, H. & Park, S. B. A comparative study of thermal fatigue life of Eutectic Sn–Bi, Hybrid Sn–Bi/SAC and SAC solder alloy BGAs. *Microelectron. Reliab.* **119**, 114065 (2021).
97. Shahapure, K. R. & Nicholas, C. Cluster Quality Analysis Using Silhouette Score. In *Proc. IEEE 7th International Conference on Data Science and Advanced Analytics (DSAA)*, 747–748 (IEEE, 2020).
98. Mei, Z., Sunwoo, A. J. & Morris, J. W. Analysis of low-temperature intermetallic growth in copper–tin diffusion couples. *Metall. Trans. A* **857**, 864 (1992).
99. Chao, B. et al. Investigation of diffusion and electromigration parameters for Cu–Sn intermetallic compounds in Pb-free solders using simulated annealing. *Acta Mater.* **55**, 2805–2814 (2007).

Acknowledgements

The authors gratefully acknowledge the financial support under the scope of the COMET programme within the K2 Center 'Integrated Computational

Material, Process and Product Engineering (IC-MPPE)' (Project No 886385). This programme is supported by the Austrian Federal Ministries for Climate Action, Environment, Energy, Mobility, Innovation and Technology (BMK) and for Labour and Economy (BMAW), represented by the Austrian Research Promotion Agency (FFG), and the federal states of Styria, Upper Austria and Tyrol, P. No. P2.22 ECOSolder. We acknowledge the support from J. Wosik for the SEM and EDX measurements and J. Magnien for stimulating discussions regarding the Cu – Sn interdiffusion.

Author contributions

C.C. performed the data-analysis work and the data interpretation and evaluation under the supervision of R.B.; F.F. developed and trained the C-DDPM with support from C.C. under the supervision of R.B.; W.H. and W.R. fabricated and provided the samples, with support from M.R. and P.I. and in discussion with C.C. and R.B.; R.B. and C.C. planned the FESEM-EBSD, FESEM-EDX; C.C. and R.B. wrote the paper with input to the model section from F.F.; All authors discussed the results and commented on the paper.

Competing interests

The authors declare no competing interests.

Additional information

Supplementary information The online version contains supplementary material available at <https://doi.org/10.1038/s41529-025-00603-9>.

Correspondence and requests for materials should be addressed to Roland Brunner.

Reprints and permissions information is available at <http://www.nature.com/reprints>

Publisher's note Springer Nature remains neutral with regard to jurisdictional claims in published maps and institutional affiliations.

Open Access This article is licensed under a Creative Commons Attribution 4.0 International License, which permits use, sharing, adaptation, distribution and reproduction in any medium or format, as long as you give appropriate credit to the original author(s) and the source, provide a link to the Creative Commons licence, and indicate if changes were made. The images or other third party material in this article are included in the article's Creative Commons licence, unless indicated otherwise in a credit line to the material. If material is not included in the article's Creative Commons licence and your intended use is not permitted by statutory regulation or exceeds the permitted use, you will need to obtain permission directly from the copyright holder. To view a copy of this licence, visit <http://creativecommons.org/licenses/by/4.0/>.

© The Author(s) 2025